Journal of Rock Mechanics and Geotechnical Engineering 17 (2025) 7711–7735

Contents lists available at ScienceDirect

Journal of Rock Mechanics and Geotechnical Engineering

journal homepage: www.jrmge.cn

Full Length Article

Design of a type of strike-slip active fault container for shaking table tests

Wenkai Feng [a, b], Lianjie Yang [b], Chunlei Xin [a, b, *], Zhao Wang [c, **], Xinyuan Yu [d], Yixin Shuai [b], Yuxin Tian [b]

[a] State Key Laboratory of Geohazard Prevention and Geoenvironment Protection, Chengdu University of Technology, 610059, Chengdu, China
[b] College of Environment and Civil Engineering, Chengdu University of Technology, 610059, Chengdu, China
[c] Institute for Transport Studies, University of Leeds, LS2 9JT, Leeds, UK
[d] School of Mechanical, Aerospace and Civil Engineering, The University of Sheffield, S10 2TN, Sheffield, UK

ARTICLE INFO

Article history:
Received 29 August 2024
Received in revised form
6 January 2025
Accepted 4 March 2025
Available online 8 March 2025

Keywords:
Shaking table tests
Fault container
Modal analysis
Hammer test
Strike-slip fault

ABSTRACT

Fault container and shaking table tests are crucial for studying co-seismic dislocation in cross-fault tunnels, with the design and functionality of the container significantly affecting the accuracy of dynamic response analyses of tunnel linings. This research introduces a fault container developed as part of a significant active fault-crossing tunnel project in the high-intensity seismic zone of western China. The container is designed to simulate both strike-slip and dip-slip fault characteristics with adjustable fault angles. Extensive testing, including shaking table tests under strong seismic conditions, three-dimensional (3D) finite element numerical simulations, and hammer tests, were conducted to evaluate the modal characteristics of the container under various conditions. The study highlights the resonance characteristics of the soil-container system, the signal consistency across different dislocations, and the dynamic response patterns both with and without pulse-like seismic motions and varying intensities. The results indicate that the natural frequencies of the container and the model soil, determined through white noise scanning, are 23.74 Hz and 6.355 Hz, respectively, suggesting no resonance in the model soil-container structure. The dynamic response characteristics of the empty container show good integrity and versatility under various seismic excitations. The consistency of the free-field time history curve confirms that the newly developed fault container effectively simulates the continuity and boundary conditions of the free-field. Time domain analysis conducted before and after fault dislocation demonstrates the capability of the container to accurately replicate the coupling effects of fault and seismic motions.

1. Introduction

Transportation tunnel projects in the high-intensity seismic zones of western China are advancing towards high-quality development. The construction of new, long, and large tunnels frequently necessitates navigating complex and challenging sections, often approaching or intersecting seismic active faults. This proximity to faults poses a significant risk of fault dislocation to tunnels during strong earthquakes, making strike-slip active faults a critical concern for the construction and maintenance of these infrastructures (Meng et al., 2024). Recent decades have witnessed severe structural damage to tunnels caused by major earthquakes. Notably, the 1995 Kobe earthquake in Japan inflicted substantial damage on 16 crossing-fault tunnels (Toda et al., 1996), while the 1999 Chi-Chi earthquake in Taiwan compromised 18 such tunnels (Yang et al., 2002). Furthermore, there were about 130 cases of crossing-fault tunnel damage as a result of the 2008 Wenchuan earthquake in China, with the Longxi Tunnel close to the Longmenshan fault zone suffering the most damage (Shen et al., 2014).

* Corresponding author. State Key Laboratory of Geohazard Prevention and Geoenvironment Protection, Chengdu University of Technology, 610059, Chengdu, China.
** Corresponding author.
E-mail addresses: xinchunlei@cdut.edu.cn (C. Xin), z.wang13@leeds.ac.uk (Z. Wang).

Peer review under responsibility of Institute of Rock and Soil Mechanics, Chinese Academy of Sciences.

https://doi.org/10.1016/j.jrmge.2025.03.001

More recently, the 2022 Menyuan earthquake in China caused thrust-type damage to the Daliang Tunnel due to the Lenglongling fault zone (Chen et al., 2023), and the 2023 Turkey earthquake caused significant damage to both crossing-fault highway and railway tunnels (Zhao et al., 2023). These incidents demonstrate the ongoing vulnerability of crossing-fault tunnels to seismic activities and highlight the importance of innovative construction and operational strategies to enhance their resilience.

The interaction between seismic motions and fault dislocation can be categorized into two types: one where active fault dislocations initiate seismic actions and another where seismic motions induce fault dislocations. Both scenarios significantly impact tunnel structures, influencing the spatial and temporal distribution of damage. Fig. 1a and b illustrates the damage resulting from the active fault dislocations initiating seismic actions affecting the Daliang tunnel during the 2022 Menyuan earthquake, which corresponds to the first type of coupling effect. This type of damage has resulted in tunnel invert uplift, lining dislocation, severe deformation, and falling blocks. Conversely, Fig. 1c and d depicts the seismic motions inducing fault dislocations that affected the Longxi tunnel during the 2008 Wenchuan earthquake, representing the second type of coupling effect. This dislocation has resulted in the collapse of the arch lining, cracking of the side walls, and falling blocks. Notably, the damage sustained by the Daliang tunnel is significantly greater than that of the Longxi tunnel. This observation suggests that the damage caused by active fault dislocation during an earthquake is more severe than that resulting from fault dislocation induced by seismic motion. This discrepancy can be attributed to the characteristics of failures caused by direct fault dislocation, which involve high energy release, high frequency, and large amplitude.

In addition, seismogenic faults result from the energy release associated with the rupture of the rock mass itself. This energy accumulation and subsequent release cause deformation in the displacement field, while the rock mass rupture leads to forced displacements. In contrast, non-seismogenic faults undergo passive displacements due to the propagation of seismic waves. The distinctions between forced and passive displacements are quite pronounced, as illustrated in Fig. 2a and b. The energy released from spontaneous fault rupture is significantly greater than that generated by far-field earthquakes. Secondly, most seismic motions associated with fault activity are classified as near-fault pulse seismic motions, which typically result in more severe damage compared to far-field earthquakes. To delve deeper into the dynamic response mechanisms of tunnel engineering under these conditions, the primary research method currently employed is shaking table tests. This approach has been widely adopted by researchers globally, prompting the design and development of specialized fault containers. These containers are instrumental in studying the coupling mechanisms between earthquakes and fault dislocations, as well as the seismic response patterns of tunnels (Xin et al., 2018).

The fault container is a critical piece of equipment in shaking table model tests of tunnel structures. Its effectiveness largely hinges on three key factors: the suitability of the dimensions of the container, the resonance issue between the model soil and container, and the boundary effects induced by the rigid material of the container (Lei et al., 2020). An important aspect to consider is the length-to-diameter ratio of the container, as an optimal ratio can effectively mitigate boundary effects (Cengiz et al., 2020). Experimental and numerical studies suggest that the dimensions of the container should generally be at least eight times the span of the tunnel to minimize the boundary effects of the soil (Xin et al., 2019). To avoid resonance, employing a generalized model based

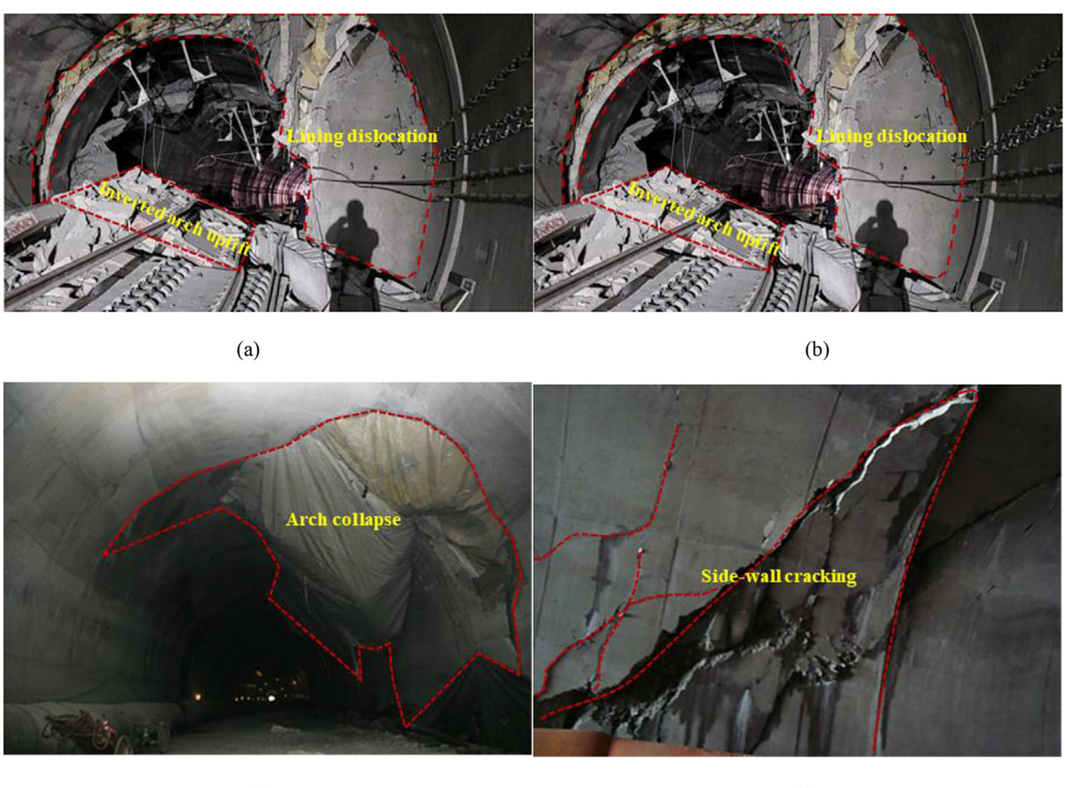

Fig. 1. Tunnel failure under different coupling effects: (a) Inverted arch uplift, (b) Lining deformation, (c) Arch collapse, and (d) Side-wall cracking.

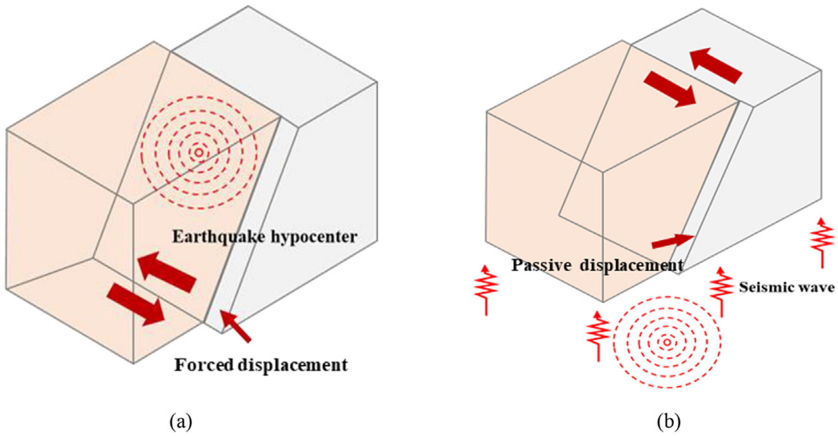

Fig. 2. Comparison of mechanisms of different coupling effects: (a) Active fault dislocations initiate seismic actions, and (b) Seismic motions induce fault dislocations.

on the shear beam method provides a theoretical framework for preventing resonance between the container and the geotechnical structure (Wang et al., 2022). Numerical research by Fishman et al. (1995) and Lombardi et al. (2015) has demonstrated that the influence of rigid boundaries can extend significantly, up to 1.5–2.0 times the depth of the soil layer. To enlarge the volume of soil experiencing free-field conditions, soft materials can be applied to the inner surfaces of the container. This approach reduces the reflection of body waves from the boundaries and also mitigates the generation of seismic waves. Additionally, flexible materials applied to the rigid boundary of the container have proven effective in diminishing boundary effects, with theoretical formulas available to guide the selection of materials for minimizing these effects in geotechnical shaking table tests (Vivek et al., 2019).

Currently, achieving fault strike-slip dislocation under static conditions is primarily done using jacks in large-scale equipment. However, this equipment is not compatible with the shaking tables, which are necessary to evaluate structural dynamic responses under dynamic conditions (Zhang et al., 2023). The use of dynamic containers in shaking table tests for tunnels crossing adverse geological sections has resolved issues such as soil-container resonance and load-bearing capacity, and validated boundary condition assumptions, while also meeting dynamic testing requirements. However, achieving multi-directional strike-slip dislocation remains a challenge (Yan et al., 2020). Hybrid tests that integrate dislocation-type rigid containers with shaking tables have further confirmed the effectiveness of fault containers in simulating the lateral deformation boundary conditions of the prototype foundation. However, these tests did not account for the effect of fault dip angle, thus failing to meet the requirements for multi-angle fault dynamic testing (Zhang et al., 2024). Additionally, model tests on the damage mechanism of hinged tunnels crossing active faults have provided detailed insights into the damage forms and mechanisms under strike-slip fault dislocation. Nonetheless, due to the limited scale of the model equipment, these tests do not accurately reflect the full-section damage of the tunnel (Cui et al., 2022b).

Shaking table tests investigating the dynamic response of tunnel lining structures to strong seismic actions triggered by strike-slip faults have revealed limitations in existing containers used to analyze the coupling effects of fault dislocation and seismic motions. To address these issues, this study introduces a novel fault container designed to simulate both strike-slip and dip-slip dislocation characteristics, with adjustable fault plane angles and dislocation velocities. Modal analysis of the container was conducted using shaking table tests and three-dimensional (3D) finite element simulations to evaluate its integrity and adaptability under various dislocations and seismic excitations. The modal properties of the container were further validated through hammer tests. Additionally, free-field shaking table tests were conducted to examine the dynamic response of the soil and validate the structural boundary conditions. The development of this testing equipment establishes a robust experimental foundation for further research. This enables a better understanding of the dynamic response characteristics of tunnel lining structures under intense seismic actions from strike-slip faults. It also aids in exploring the seismic damage mechanisms of tunnels crossing active faults, particularly in high-intensity seismic areas where earthquakes and dislocations occur simultaneously.

2. Fault container design

2.1. Detailing requirements

To accurately simulate the propagation of one-dimensional (1D) shear waves in soil samples with finite thickness, the container must incorporate specific key modeling attributes. Han et al. (2020) identified several critical standards necessary for an ideal container to accurately simulate the boundary conditions of soil in an infinite lower layer:

(1) *Size and Structural Integrity*: The frame must be appropriately sized and structurally robust to prevent any lateral expansion or contraction during vibrations.
(2) *Structural Stiffness and Weight*: Within the constraints of its dimensions, the container should maximize structural stiffness while minimizing its weight as much as possible.
(3) *Inertial Forces*: The inertial forces from the container's mass should not affect the vibration response of the model soil.
(4) *Seismic Response Simulation*: During dislocation, the interaction between the model soil and the container should closely replicate actual seismic response conditions.
(5) *Lateral Boundary Simulation*: The container must accurately simulate the lateral boundary conditions of the model soil.
(6) *Resonance Prevention*: The design should avoid resonance by ensuring the container's natural frequencies do not align with those of the model soil.
(7) *Load-Bearing Capacity*: The container must be designed with sufficient load-bearing capacity to prevent damage during

experiments, ensuring durability and stability throughout testing.

These criteria will ensure that the container provides a reliable and realistic simulation environment for studying soil behavior under seismic conditions.

2.2. Design and manufacture of container

The selection of material for the fault container is crucial for ensuring its reliability. Consequently, Q345 steel was selected for its construction. This custom-designed fault container consists of three primary structural components: the hanging wall cabinet, the footwall cabinet, and the power device. To accurately simulate seismic responses, it is essential that the boundary conditions of the model soil replicate the deformation mode of actual soil, thereby preventing seismic energy reflection from rigid boundaries. To achieve this, a 10 cm thick foam plastic panels are installed along the interior transverse sidewalls of the container (Xin et al., 2020).

The design of the container can directly affect the reliability of dynamic response data for tunnel structures. Therefore, a fault container was engineered to emulate both strike-slip and dip-slip characteristics of faults, featuring adjustable fault plane angles. The container consists of a hanging wall cabinet, a footwall cabinet, a fault angle adjustment disk, a system control panel, crossbars, and a bottom plate, with overall dimensions of 3.7 m × 1.5 m × 1.9 m (length × width × height), as shown in Fig. 3a and b. Constructed from a steel frame, the container integrates the hanging wall and footwall sections, connected via a bottom plate as illustrated in Fig. 3c. These sections are supported by side panels and transverse beams, which define the container space. The hanging wall and footwall sections are designed to slide horizontally or at an incline in one or both directions along the fault plane through a dynamic dislocation device. Furthermore, the rotating disk on the adjustment structure (Fig. 3d) is connected to the hanging wall and footwall sections via high-strength bolts, facilitating the adjustment of fault plane angles. This configuration, aligned with actual geological conditions, allows for the exploration of how variations in dip-slip fault angles influence the structural dynamic response of tunnels crossing faults.

3. Shaking table test preparation

3.1. Input seismic excitation scheme

This study was organized into two groups of tests. The first group involved tests with an empty container to assess the consistency of various modal characteristics and the dynamic responses of the fault container. The second group, a free-field test, utilized model soil within the container to validate its boundary conditions and to examine the effectiveness of the coupling effects between different types of fault dislocation and seismic motions. Notably, the coupling effects of actual seismic motion and fault dislocation exhibit distinct characteristics. Two types of coupling effects were considered for the selection of seismic motions: the first type involves seismic coupling effects initiated by active fault dislocation, while the second type relates to fault dislocation induced by seismic motion. For the former, seismic motions characterized by pulse effects were chosen, such as the Menyuan (MY) seismic motion. This motion is known for its pulse and narrow frequency characteristics, which were instrumental in the damage to the Daliang tunnel due to strong seismic actions triggered by the transient dislocation of the seismogenic fault (Chen and Liu, 2019). The test setup for this type involved simultaneous fault dislocation and seismic action. The latter type selected non-pulse effect seismic waves, such as the Wolong (WL) seismic motion, which is characterized by the absence of pulse and narrow frequency. This motion caused damage to the Longxi tunnel due to the dislocation induced

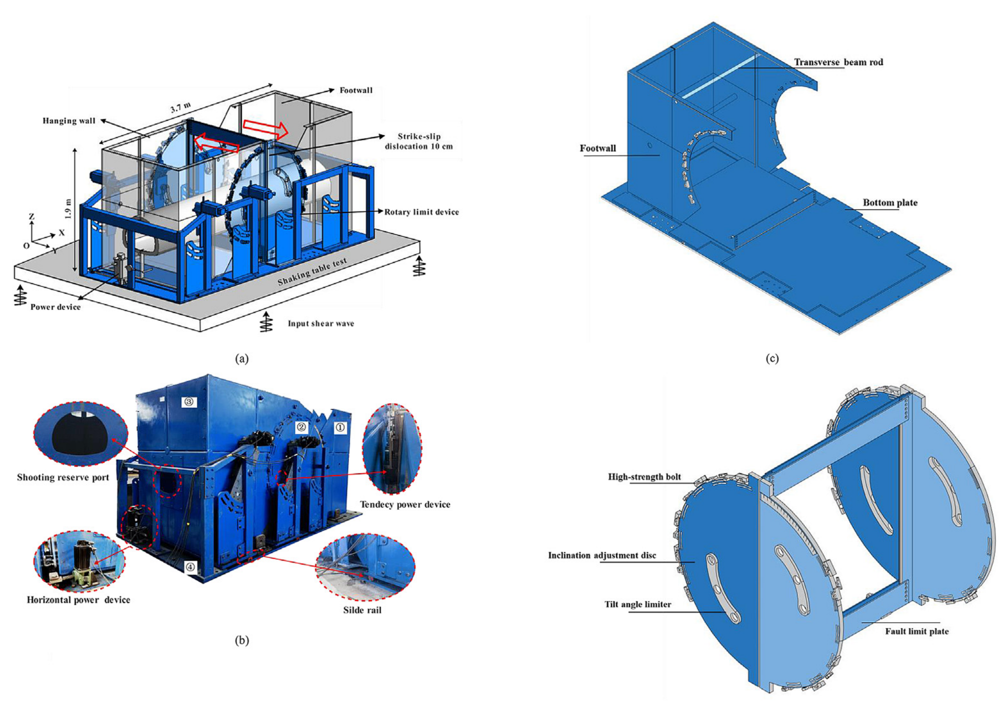

Fig. 3. Rigid fault container: (a) 3D schematic diagram of rigid fault container; (b) Physical fault container; (c) Detailed diagram of the footwall frame; and (d) Detailed diagram of the angle adjustment disk.

by the seismic waves during the Wenchuan earthquake (Xin et al., 2022). In this case, the seismic action was applied first, followed by the fault dislocation consideration. In addition, a shaking table free-field test was carried out to verify the boundary effects of the container and to investigate the deformation behavior of the model soil within it. The specific loading conditions for the model tests are presented in Table 1. The acceleration time history curves and Fourier spectra of the two seismic motions are shown in Fig. 4.

3.2. Monitoring scheme

To investigate the dynamic response characteristics and modal properties of the container in test group 1, acceleration sensors were employed to monitor dynamic signal responses at the boundaries and fault locations of the fault container. Sensors A01 through A08 were positioned at the boundaries to assess the overall performance. Sensors A09 and A10 were strategically positioned at the fault junction to examine and verify the consistency of the acceleration response. The detailed monitoring arrangement for test group 1 is shown in Fig. 5a and b.

To validate the effectiveness of the novel fault container in test group 2, yellow sand in its natural state was utilized as the model soil for free-field test. The free-field response characteristics were identified by analyzing the acceleration and dislocation responses of the model soil. A longitudinal cross-section along the central line of the model soil was determined as the reference monitoring plane to deploy accelerometers and displacement sensors. The specific arrangements of the acceleration sensors (denoted by the letter A) and the locations of the laser displacement gages (denoted by the letter D) are illustrated in Fig. 6a and b. Accelerometers placed at the model's boundaries and central region were employed to investigate and validate the boundary conditions of the container. Accelerometers situated near the fault were utilized to analyze the dynamic response patterns of the free field, as well as the fault strike-slip behavior on both the hanging wall and footwall. Displacement gages positioned at the tops of the hanging wall and footwall were used to measure the surface settlement of the model soil.

To mitigate the impact of the rigid boundaries of the fault container, 10 cm thick foam panels were installed along both the lateral and longitudinal boundaries inside the container. The model soil was subsequently filled in layers, each measuring 20 cm in thickness. After the layering was complete, sensors were embedded according to the monitoring plan. To secure the sensors during the experiment and ensure accurate signal measurements, the surrounding soil was compacted. The final height of the model soil in the container reached 1.6 m. Grid lines were drawn on the soil surface to monitor deformation characteristics. Once the filling process was completed, the setup was allowed to stabilize for 24 h before initiating the shaking table tests. The detailed construction process is shown in Fig. 7.

4. Analysis of shaking table test results

4.1. Analysis of white noise results

Acceleration response data from multiple measuring points, including A01, A04, A05, A08, and A09, located at the boundaries and fault position within the fault container were collected using the frequency sweep method. Since the frequency range of seismic motion signals is 0–100Hz, a band-pass filtering method with a frequency threshold range of 0-60 Hz was employed to eliminate experimental noise and instrumental errors during the tests. To analyze the frequency response of the container, the filtered acceleration signals were subjected to Fourier transformation. The frequency domain Fourier spectra were subsequently smoothed to refine the frequency spectrum, as shown in Fig. 8.

As shown in Fig. 8, the response frequencies and amplitude peak values at the measurement points A01, A04, A05, A08 and A09 are (22.25 Hz, 0.016 g/Hz), (22.21 Hz, 0.018 g/Hz), (24.06 Hz, 0.085 g/Hz), (24.84 Hz, 0.10 g/Hz), and (25.36 Hz, 0.12 g/Hz), respectively. These data show significant variations in the frequency spectrum characteristics between different measurement points at the top and bottom of the container. The amplitude at the top is greater than that at the bottom, which can be attributed to the bottom of the container being more rigidly constrained by the shaking table surface, resulting in lower amplitude peaks. In contrast, the top of the container, being a freer surface with less constraint and more degrees of freedom, exhibits higher amplitude peaks. This phenomenon, known as "elevation amplification," occurs as seismic waves propagate within the container. Furthermore, monitoring data reveal higher natural frequencies measured at the junction of the hanging wall and the footwall of the fault. This can be attributed to the necessity of simulating the fault strike-slip dislocation within the container model, which possesses a higher degree of freedom and is more susceptible to external perturbations. Consequently,

Table 1
Shaking table container tests case table.

Type	Test case	Dislocation (cm)	Input seismic motion	Direction	Peak acceleration (*g*)
Test group 1	Case-1	0	White noise	*Y*	0.2
	Case-2		Menyuan	*Y*	0.4
	Case-3		Menyuan	*Y*	1.0
	Case-4	0	White noise	*Y*	0.2
	Case-5		Wolong	*Y*	0.4
	Case-6		Wolong	*Y*	1.0
	Case-7	5	White noise	*Y*	0.2
	Case-8		Menyuan	*Y*	0.4
	Case-9	10	White noise	*Y*	0.2
	Case-10		Menyuan	*Y*	0.4
Test group 2	Case-11	0	White noise	*Y*	0.2
	Case-12		Menyuan	*Y*	0.4
	Case-13		Menyuan	*Y*	1.0
	Case-14	0	White noise	*Y*	0.2
	Case-15		Wolong	*Y*	0.4
	Case-16		Wolong	*Y*	1.0
	Case-17	10	White noise	*Y*	0.2
	Case-18		Menyuan	*Y*	0.4
	Case-19		White noise	*Y*	0.2

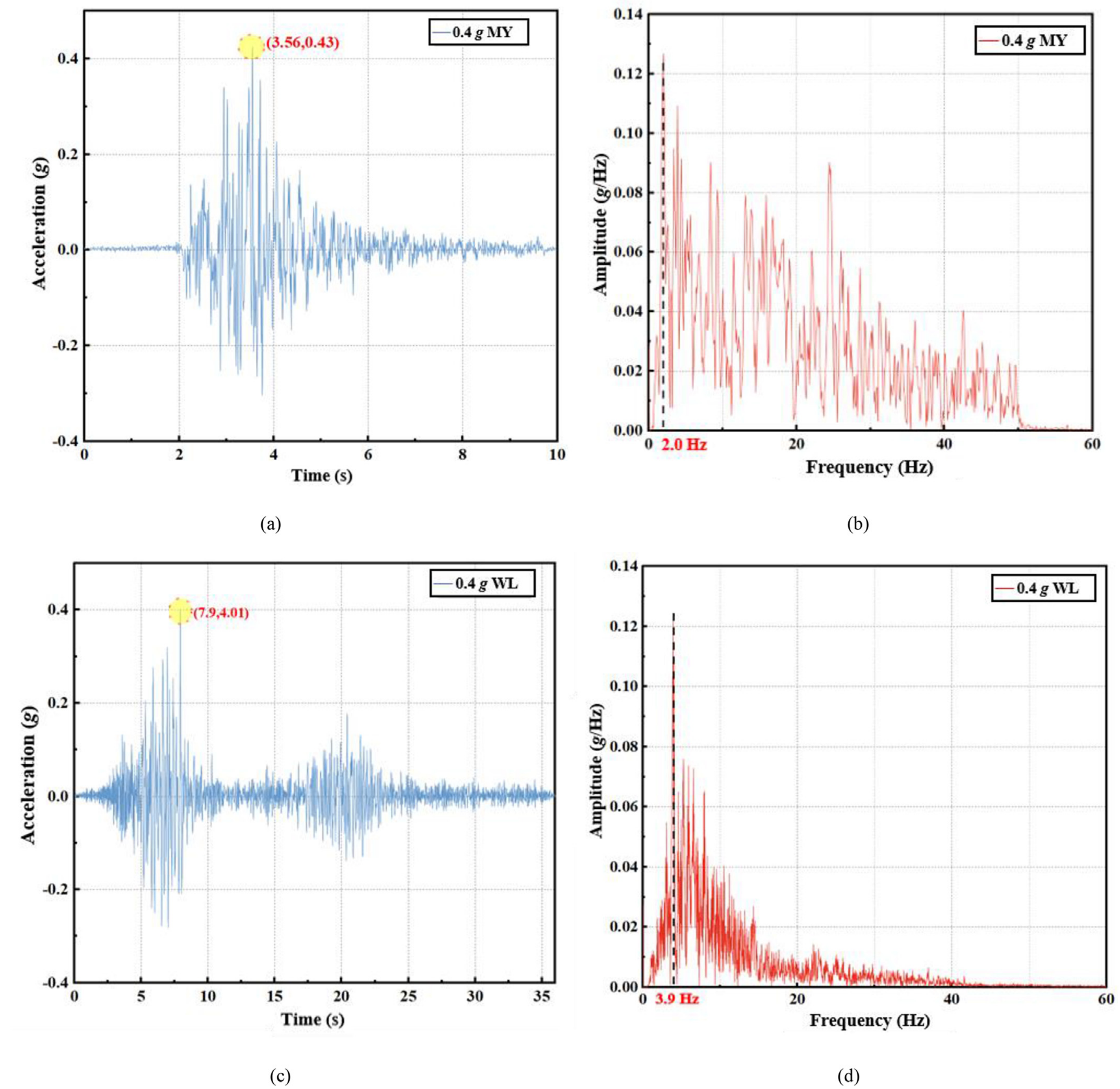

Fig. 4. Input seismic motion acceleration time history and Fourier spectrum of shaking table model tests: (a) 0.4 *g* MY acceleration time history curve; (b) 0.4 *g* MY Fourier spectrum; (c) 0.4 *g* WL acceleration time history curve; and (d) 0.4 *g* WL Fourier spectrum.

this results in a higher measured natural frequency at the junctions between the hanging wall and the footwall of the fault, suggesting the suitability of the container for fault characteristics analysis. Overall, the arithmetic mean of the frequency values obtained from the measurement points suggests a natural frequency of 23.74 Hz for the container, providing a crucial analytical basis for evaluating the suitability of the container in shaking table tests and the validity of numerical simulations.

To mitigate the impact of the container's natural frequency on the shaking table model tests, it is essential to minimize resonance between the model material and the container during the experiments. Yan et al. (2019) studied model soils composed of Class V surrounding rock materials for mountain tunnels crossing poor geological sections, identifying a natural frequency of 8.62 Hz. In contrast, Zhang et al. (2019) conducted shaking table tests to assess the dynamic response of tunnel junctions in soft soil under lateral excitation, finding a natural frequency of 11.43 Hz for the model soil. Table 2 presents a summary of the natural frequencies of various model soils utilized in shaking table tests. The natural frequency of the custom-designed fault container is more than twice that of the model soils discussed, demonstrating the container's strong suitability for these tests.

White noise excitation was utilized to determine the fundamental frequency of the model soil in test group 2. Fig. 9a and b

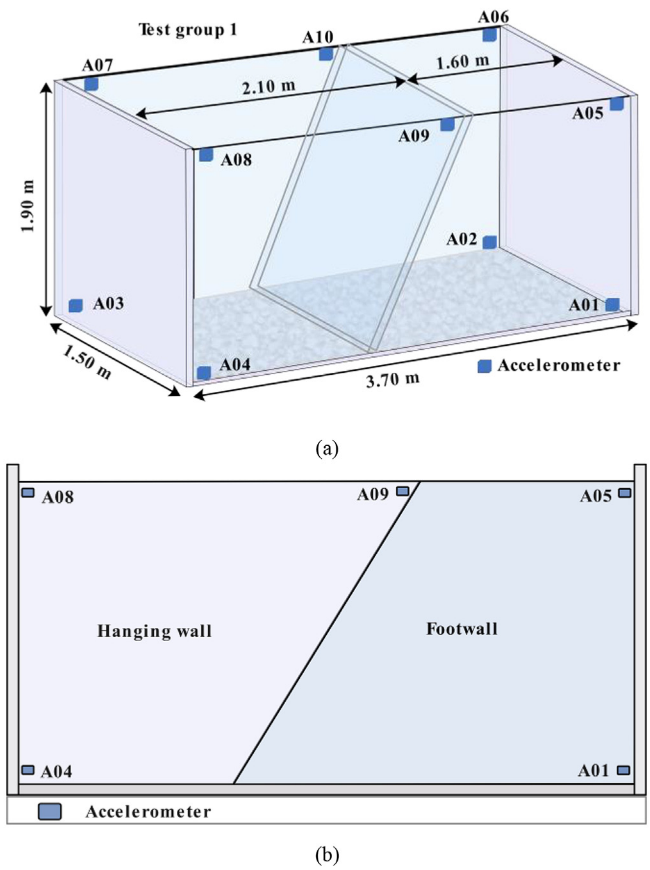

Fig. 5. Accelerometer arrangement for test group 1: (a) 3D view of accelerometer arrangement; and (b) Plan view of accelerometer arrangement.

displays the Fourier spectra of accelerations at sensors A31 and A34 under white noise cases 11 and 14, respectively. The initial white noise scan identified the natural frequency of the model soil as 6.355 Hz, aligning with the natural frequencies of commonly used model soils listed in Table 2, thereby confirming the reasonableness of the model soil in test group 2. The Fourier spectra from various positions before fault dislocation exhibit notable consistency, indicating the overall integrity of the container. Simultaneously, the fundamental frequency of the model soil increased from 6.355 Hz to 6.763 Hz between case 11 to case 14, accompanied by a decrease in amplitude. Following fault dislocation, from case 17 to case 19, the fundamental frequency showed a similar pattern of change. This is attributed to the increased density of the soil resulting from the seismic motion effects. Notably, after fault dislocation, the model soil experienced a reduction in density leading to a decrease in its fundamental frequency, as shown in Fig. 9c and d. The fundamental frequency of the hanging wall rose from 5.013 Hz to 6.88 Hz, whereas that of the footwall increased from 5.013 Hz to 8.974 Hz. The higher fundamental frequency of the footwall compared to the hanging wall is due to the hanging wall acting as an active block, more susceptible to fracture, while the footwall is vulnerable to densification during excitation. In summary, the fundamental frequency of the model soil and the container differed by more than a factor of 2 both before and after fault dislocation, effectively avoiding resonance phenomena. This further confirms the rationale behind the design of the container.

To investigate the frequency-domain response characteristics of rock masses at different elevations under various seismic excitations prior to fault dislocation, a primary frequency range of 0-20 Hz was selected for analyzing Menyuan and Wolong seismic motions. This selection is based on the dominant frequency range of both natural seismic motions, which typically fall within 15 Hz. The Fourier spectra from the model soil at the top (A51) and bottom (A15) under these seismic excitations are shown in Fig. 10a and b. The peak values at different elevations correspond closely to the same fundamental frequency of the sandy soil surface, demonstrating that the container maintains good integrity during seismic motion excitation. Notably, the amplitude increases with elevation, attributed to the greater energy of seismic motions at higher elevations (Xin et al., 2024b). Furthermore, the frequency response under both types of seismic excitations centers around 7 Hz, reinforcing the reliability of the experimental data and the reproducibility of the tests. It is noteworthy that within the range of 0-5 Hz, there are slight differences in the response of frequency spectrum of the model, with the impact of Menyuan seismic motion being

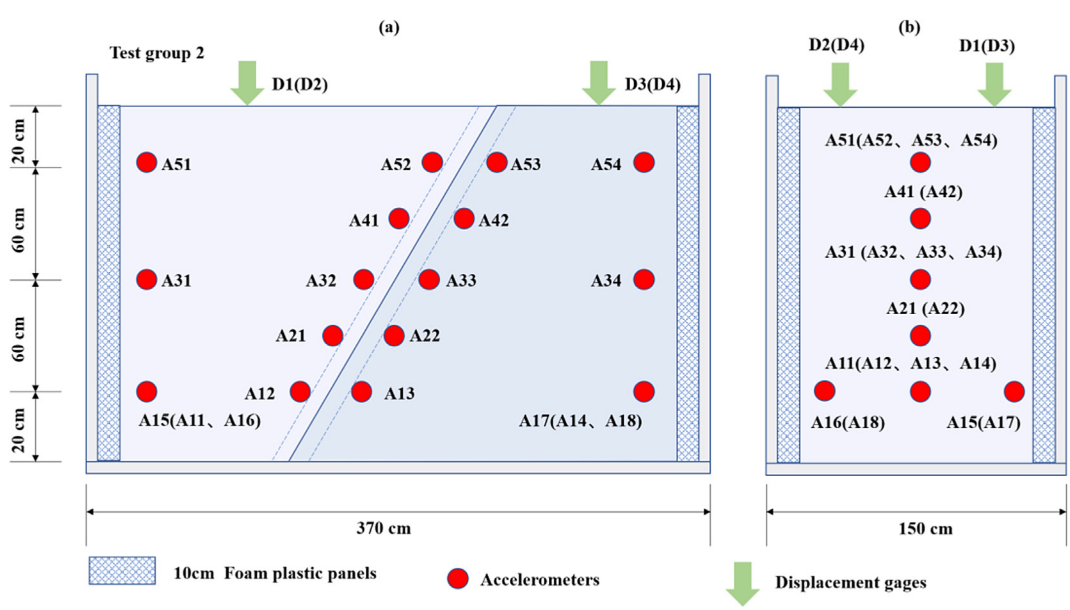

Fig. 6. Monitoring scheme for test group 2: (a) Schematic diagram of sensor arrangement; and (b) Side view of sensor arrangement.

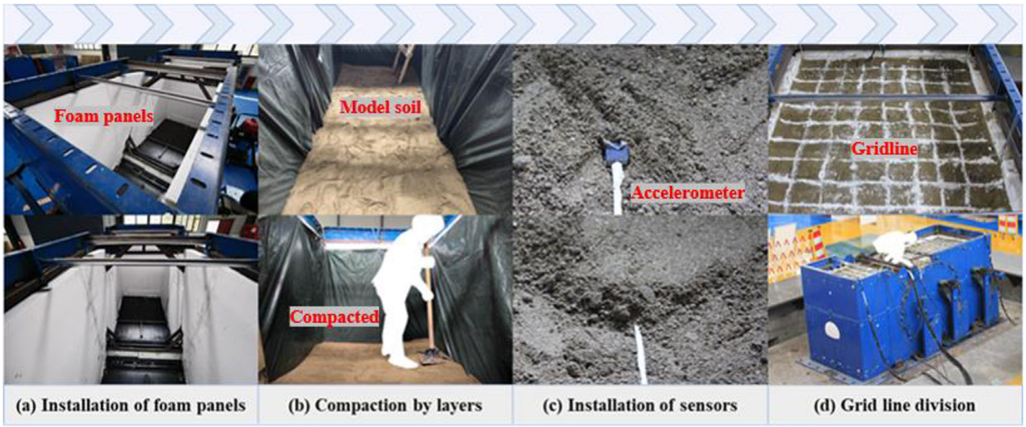

Fig. 7. The specific construction process for test group 2.

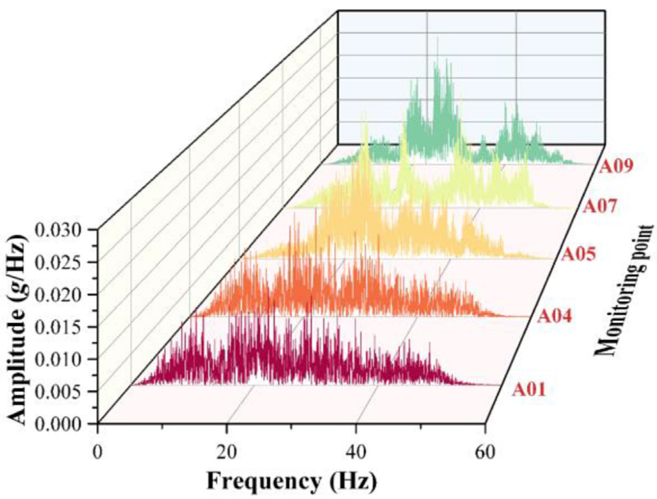

Fig. 8. Measuring point acceleration spectrum diagram.

greater than that of Wolong seismic motion. This is due to Menyuan seismic motion having a higher amplitude in the 0–20 Hz frequency range (Fig. 4b). However, since these discrepancies are minor and occur in a frequency range significantly different from the model soil's fundamental frequency, they are considered negligible. Moreover, the fundamental frequency of the model soil differs by more than a factor of 2 from the container's natural frequency, ensuring that under normal experimental conditions, the container does not resonate with the model soil, thus meeting the experimental requirements effectively.

4.2. Response signal consistency analysis

Due to the smaller scale of the model tests compared to the actual geological environment, no significant differences were observed in signal responses at the boundaries, highlighting the substantial impact of the container's overall integrity on the model tests. Therefore, three fault dislocation scenarios were implemented to assess this impact: no dislocation, 5 cm dislocation, and 10 cm dislocation. The consistency of the response signals at various measurement points within the container is critical for validating the overall design integrity of the container and the reliability of the model tests. Fig. 11 presents the acceleration time histories and Fourier spectra from sensor A07 under different fault dislocation scenarios with Menyuan seismic motion excitation.

As shown in Fig. 11a, the signal waveforms at measurement point A07 exhibit a high degree of similarity across fault

Table 2
Natural frequency of common model soil.

Research object	Similarity ratio	Prototype material	Molding material	Natural frequency of model soil (Hz)
Mountain tunnel	$C_l = 1:30$ $C_\rho = 1:1.5$ $C_e = 1:45$	Class V surrounding rock	Baryte powder, quartz sand, gypsum, laundry detergent, water	8.62
Shaft tunnel	$C_l = 1:60$ $S_a = 4:1$	Undisturbed soil	Wood chips, dry sand	11.43
Slope reinforcement with anchored piles (Hu et al., 2023)	$C_l = 1:25$ $C_\rho = 1:1$ $C_e = 1:25$	Rocky soil	Baryte powder, quartz sand, gypsum, water	6.78
Tunnel portal slope (Wang et al., 2023a)	$C_l = 1:40$ $C_\rho = 4:5$ $C_e = 1:40$	Class V surrounding rock	Fly ash, river sand, engine oil, soil	8.37
Bedding rock slope (Wu et al., 2020)	$C_l = 1:100$ $C_\rho = 1:1$ $C_e = 1:100$	Siliceous slate	Baryte powder, quartz sand, glycerin, gypsum, water	2.54
Immersed tunnel (Chen et al., 2017)	$C_l = 1:60$ $C_\rho = 13:20$ $C_e = 1:12.4$	Undisturbed soil	Sawdust, clay	7.81

Note: C_l is length similarity ratio, C_ρ is Density similarity ratio, C_e is shear modulus similarity ratio, S_a is acceleration similarity ratio.

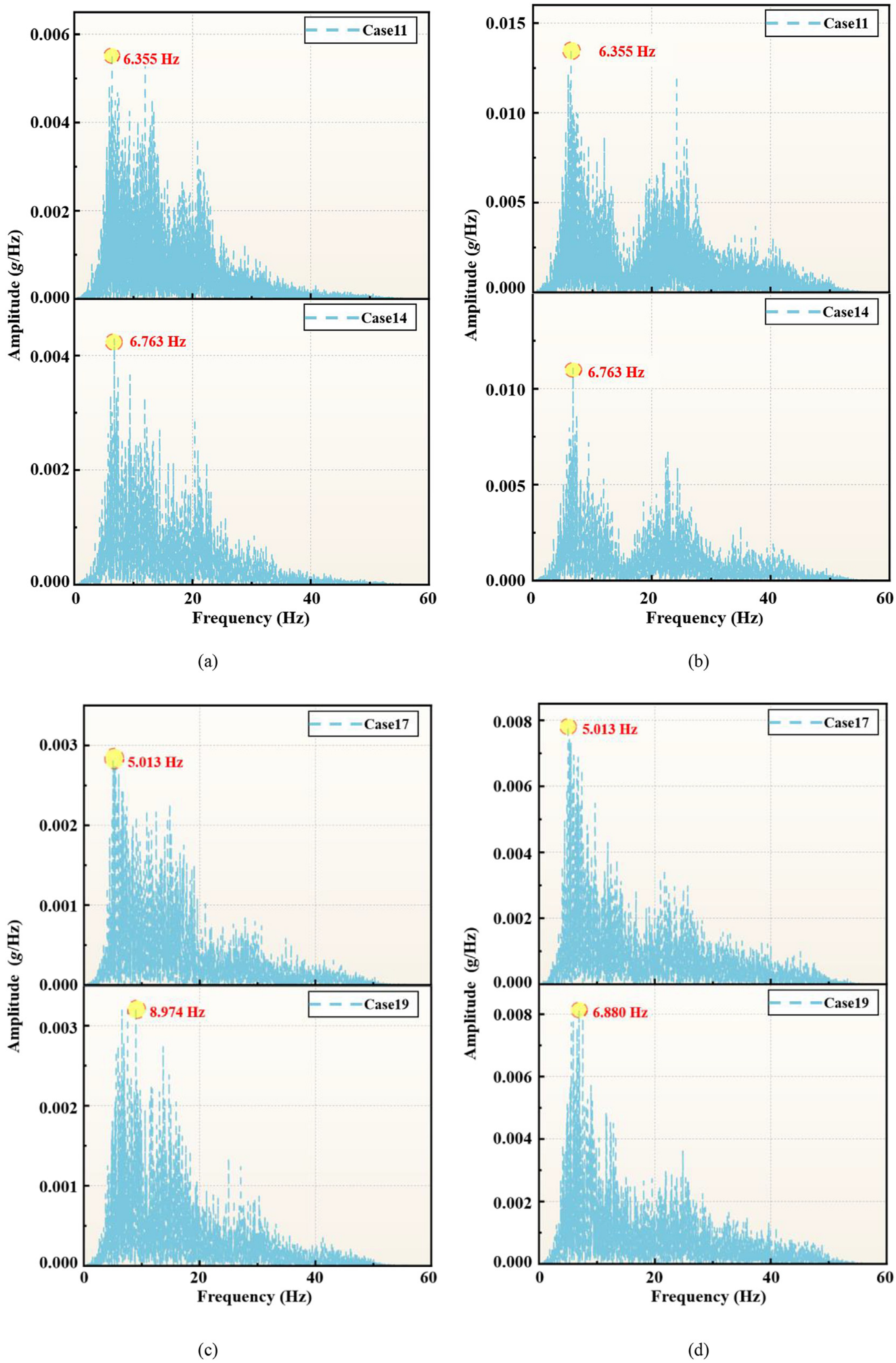

Fig. 9. Comparison of Fourier spectra under different cases and positions: (a) Before fault dislocation A31; (b) Before fault dislocation A34; (c) After fault dislocation A31; and (d) After fault dislocation A34.

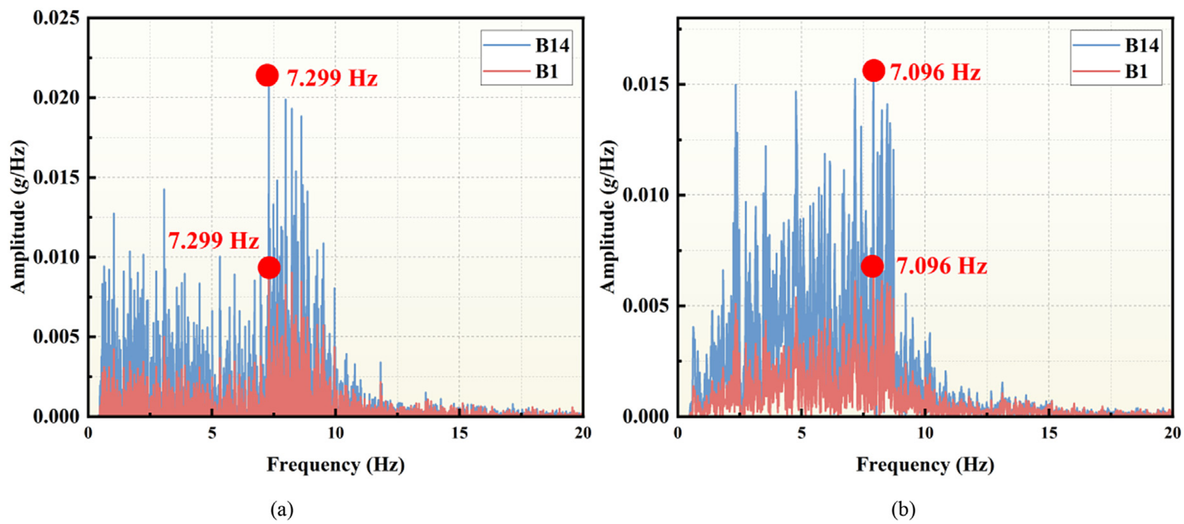

Fig. 10. Comparison of Fourier spectra for different seismic motions: (a) 0.4 *g* MY seismic motion; and (b) 0.4 *g* WL seismic motion.

dislocations, indicating that the container maintains good overall integrity and adaptability under varying fault dislocations. Additionally, under different dislocation cases and consistent seismic motion excitation, the peak acceleration at this location increases with the extent of fault dislocation. This increase is attributed to intensified fault activity within the container as the dislocation widens, amplifying the response to seismic excitation at that specific point. In real-world scenarios, mountain tunnels subjected to strong seismic activity due to active fault strike-slip can cause the rock mass structure to fracture and release energy. Therefore, larger dislocation results in greater energy release, which is consistent with the observation from the shaking table model tests where increased fault dislocation leads to larger signal responses. This consistency suggests that the container effectively simulates the coupling effects between strike-slip faults triggering strong seismic actions. Fig. 11b shows that the Fourier spectra also exhibit

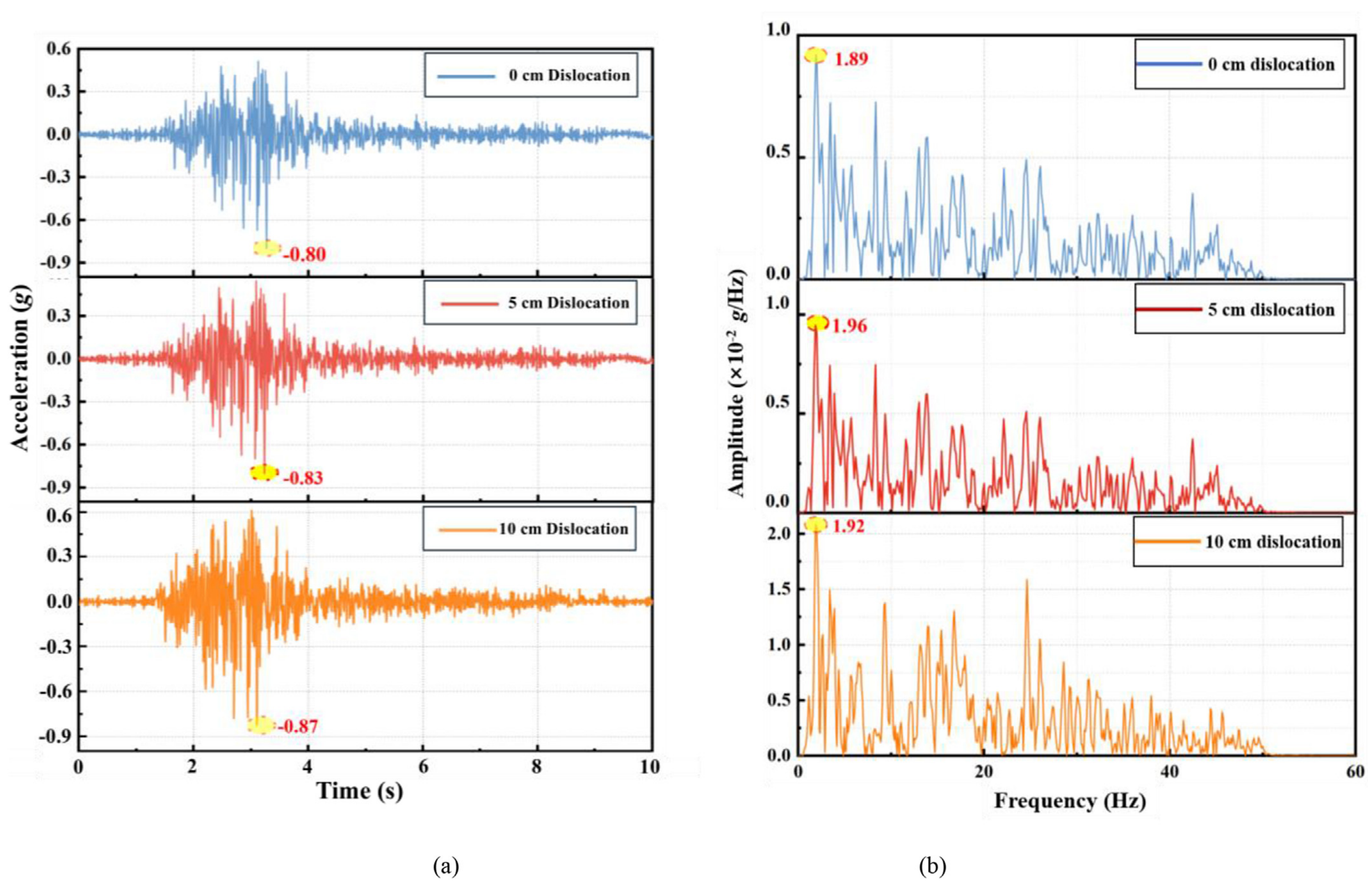

Fig. 11. Acceleration time history and Fourier spectrum at different dislocation: (a) Acceleration time history curve; and (b) Fourier spectrum.

consistency in frequency spectrum under different fault dislocations. Moreover, as dislocation increases, the energy of the signal response intensifies, influencing the dominant frequency of the seismic motions due to larger dislocations correlating with greater strain energy release. The container design incorporates fault tolerance and adaptability, allowing it to accommodate changes within a specified range without significantly affecting overall performance.

4.3. Dynamic response analysis under different seismic excitations

To further investigate the adaptability of the container and the dynamic response characteristics at each measurement point under different seismic motions, Fig. 12 shows the acceleration time history curves at different measurement points under various intensities of Menyuan seismic motion and Wolong seismic motions.

As shown in Fig. 12a and c, under the same peak acceleration excitation, the acceleration peaks at measurement points A01 and A05 show nonlinear amplification, exhibiting an elevation amplification effect. This behavior is consistent with real-world conditions and confirms that the container accurately simulates the propagation of seismic motions. Specifically, the amplification factor for Menyuan seismic motion is 1.84, while for Wolong seismic motion it is 2.44. In test group 1, the amplification effect caused by Wolong seismic motion is more pronounced than that caused by Menyuan seismic motion. The consistency of waveforms further demonstrates the container's robust applicability and its ability to simulate the coupling between different types of seismic motions and fault dislocation. Fig. 12a–d shows that for the same type of seismic motion, an observable amplification effect occurs with increasing height; the higher the acceleration amplitude, the more pronounced the amplification effect. Furthermore, it is observed that the time history curve of the input base acceleration closely aligns with the time history curve of acceleration measured at A01, with an error margin within a reasonable 2%. The consistency of waveforms at different measurement points within the container also attests to its overall integrity. Moreover, as shown in Fig. 12a–d, the acceleration response at the same location significantly increases with rising peak acceleration, and the energy levels also increase. This phenomenon is attributed to the inherent amplification effect of seismic wave energy at different peak levels, which is consistent with the observations obtained from the seismic excitation of the container. This further demonstrates that the container effectively simulates the dynamic response following seismic excitation.

As shown in Fig. 13a and b, the amplification coefficient of the table surface remained essentially constant as the excitation intensity increased, approximately equal to 1.0. To quantitatively characterize the variation in acceleration within the container under the excitation of seismic waves with different peak ground accelerations (PGA), the acceleration amplification factor (AAF) is introduced to describe the amplification effect. The AAF is defined as the ratio of the PGA at the monitoring location to the input peak acceleration of the seismic motion. From the observation of Fig. 13, it can be seen that under the same type of seismic loading conditions, the acceleration amplification factor increases with the rise in peak acceleration. Furthermore, the rate of increase in the acceleration amplification factor also accelerates with increasing elevation, which is consistent with theoretical principles. Notably, under different seismic excitation conditions at the same peak acceleration, the AAF at the same monitoring location for the Wolong wave is consistently greater than that for the Menyuan wave. In summary, the container does not affect the effective transmission of seismic wave energy, demonstrating that it meets the requirements for shake table tests. Additionally, under the 1.0 *g* seismic wave excitation conditions, the model container showed no signs of instability or significant deformation, indicating that it possesses a strong dynamic load-bearing capacity.

To verify the adaptability of the container under various coupling effects, Fourier spectrum comparisons were conducted using different intensities of Menyuan seismic motion, Wolong seismic motion, and white noise. The influence of these different seismic motions on the natural frequency of the container at the same measurement point A05 was analyzed, as shown in Fig. 14.

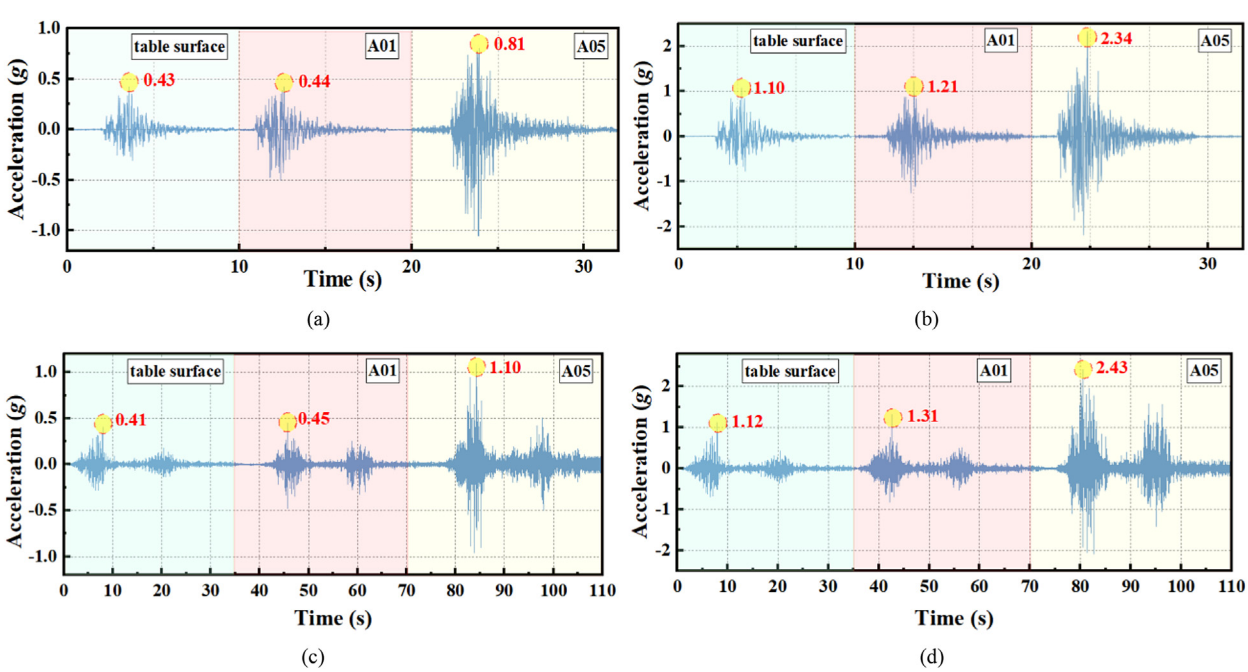

Fig. 12. The acceleration time history curves of each measuring point under different excitation amplitude values and seismic motions: (a) 0.4 *g* MY Acceleration time history curve; (b) 1.0 *g* MY Acceleration time history curve; (c) 0.4 *g* WL Acceleration time history curve; and (d) 1.0 *g* WL Acceleration time history curve.

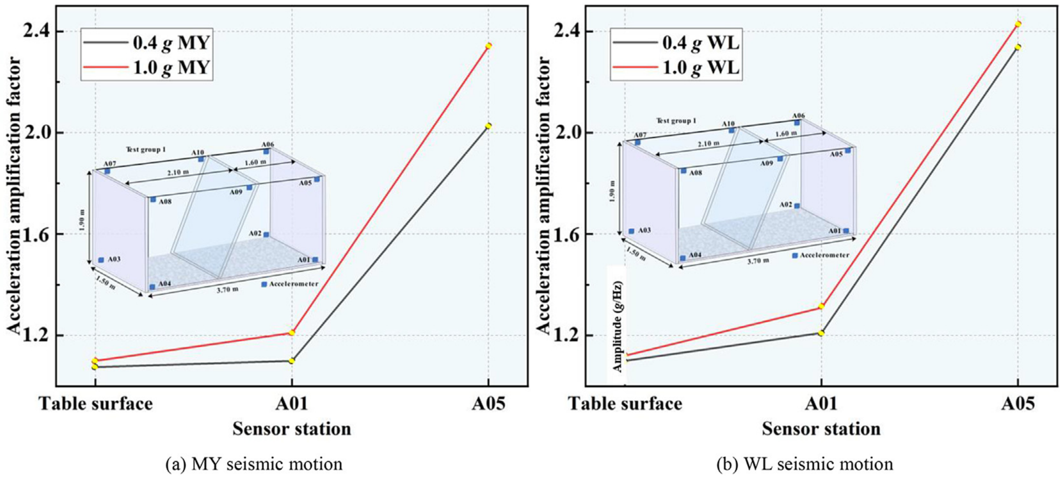

Fig. 13. Comparison of acceleration amplification coefficients under different peak acceleration conditions.

Fig. 14a and b shows significant differences in the spectral characteristics of the container under different seismic excitations. In these figures, area 1 denotes the first natural frequency of the container, while area 2 represents the response of the container at other frequencies under seismic excitation. The natural frequency of the container is notably higher than the dominant frequency of the input seismic motions, which helps prevent resonance phenomena. The maximum frequency response of the container under various seismic excitations is primarily governed by the dominant frequency of the input seismic motions, illustrating that the dominant frequency of natural seismic waves is considerably lower than the container's natural frequency. Analysis of the frequency response amplitude reveals that at the same peak acceleration amplitude, the energy imparted by Wolong seismic motion is significantly higher than that from Menyuan seismic motion. Consequently, the amplification effect induced by Wolong seismic motion is more pronounced. This difference further underscores the complex interactions between the spectral characteristics of the seismic motions and the vibrational response of the container, encompassing energy transfer and nonlinear effects. Moreover, under seismic wave excitations, the container exhibits responses in other frequency bands rather than its own dominant frequency. As a complex structural system, the fault container likely possesses multiple natural frequencies. However, although container possesses multiple natural frequencies due to its complex design, the tests and simulations primarily focus on identifying the fundamental frequencies associated with the most dominant vibration mode under the specific conditions applied during shaking table tests. The single frequency measured does not negate the existence of higher-order modes, rather, it reflects the specific excitation conditions applied. The measured modes following seismic excitation are related to the input load, the distinction between real seismic motion and white noise is evident in their frequency domain power spectra. The power spectrum of all frequency components of white noise is relatively uniform, while real seismic motion exhibits a more pronounced power spectrum within specific frequency ranges. Thus, when the resonance frequency is closely aligned with the dominant frequency of seismic motion, the corresponding mode becomes more pronounced, whereas other modes may be less distinct. In other words, when the frequency of the applied seismic motion approaches or coincides with one of these natural frequencies, it can trigger a spontaneous vibration, known as the “resonance effect,” leading to an intensified vibrational response in the container. This dynamic underscore the critical need for careful consideration of the container's design and the selection of seismic inputs to avoid unintended resonance.

4.4. Boundary effects of modeled soil container

The conventional method for evaluating boundary effects in soil

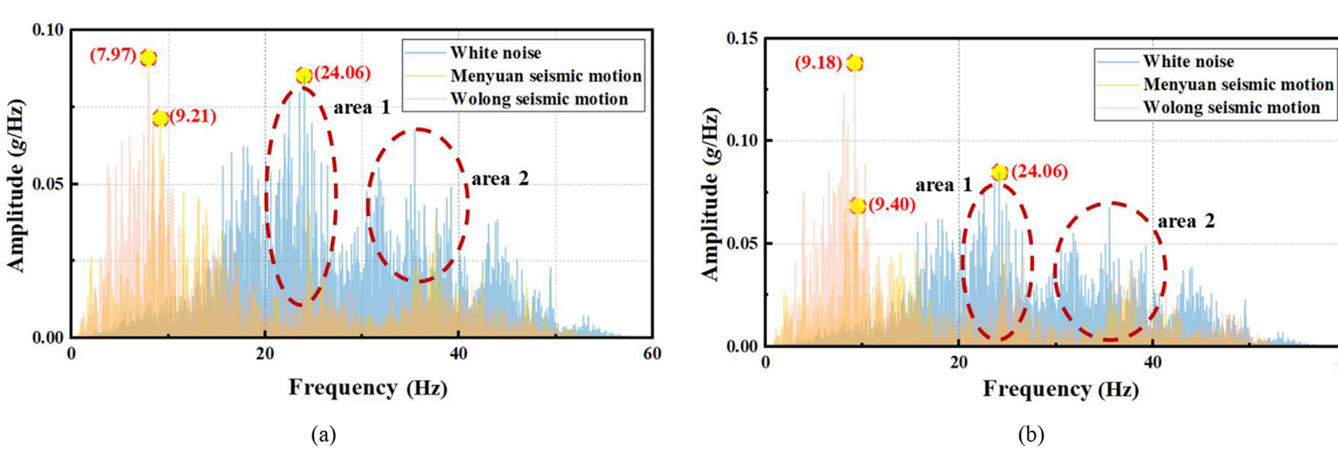

Fig. 14. Fourier spectrum under different seismic motion: (a) 0.4 *g* Fourier spectrum; and (b) 1.0 *g* Fourier spectrum.

containers involves using the vibration response at the center of the soil model as a reference. This response is then compared with the vibration responses at other monitoring points located near the boundary at the same elevation (Li et al., 2020). Boundary effects are typically calculated by comparing the ratio of two signals, where a ratio closer to 1 indicates a smaller boundary effect. For instance, under 0.4 *g* excitation from Menyuan seismic motion, the acceleration time histories of central and boundary sensors at different dislocations and elevations were collected from test group 2, as shown in Fig. 15.

As shown in Fig. 15a and b, a comparison of the acceleration time histories of measurement points A14 and A17, as well as A13 and A14, shows that the responses are nearly identical in both the longitudinal and transverse directions. This consistency demonstrates that the container meets the boundary conditions for both directions under seismic excitation cases. Fig. 15b–d shows that the acceleration time histories recorded at different elevations are similar. This suggests that the container satisfies the boundary conditions at different elevations during non-dislocation cases. Although a slight amplification was observed at the boundary monitoring points, the errors remained within 3% margin, which is acceptable for experimental purposes and can be considered negligible. Additionally, boundary conditions for the hanging wall and footwall of the container were assessed during the seismic fault dislocation process, as shown in Fig. 15e and f. The results confirm that both the hanging wall and footwall of the container satisfy the boundary conditions post-fault dislocation. This also validates that the container can simulate the coupling between active faults and seismic motion. It is noteworthy that the acceleration response of the hanging wall is greater than that of the footwall, aligning with theoretical expectations (Li et al., 2024). This outcome further confirms the reliability and effectiveness of the container design.

To further validate the rationality of the boundary conditions, a quantitative analysis of the boundary effects at the model monitoring points is conducted. This analysis utilizes the Pearson product-moment correlation coefficient (r) and 2-norm deviation (μ) to examine the correlation and deviation between measurement points A34 and A33. This statistical approach helps quantify the degree of similarity and the consistency of the responses across these points.

$$r=\frac{Cov(X,Y)}{\sqrt{Var(X)Var(Y)}}=\frac{\sum_{i=1}^{n}(x_i-\overline{x})(y_i-\overline{y})}{\sqrt{\sum_{i=1}^{n}(x_i-\overline{x})^2\sum_{i=1}^{n}(y_i-\overline{y})^2}} \tag{1}$$

$$\mu=\frac{\|x_i-y_i\|}{\|x_i\|}=\sqrt{\frac{\sum(x_i-y_i)^2}{\sum(x_i)^2}} \tag{2}$$

where, x_i is the reference signal and y_j is the comparison signal. x_i and y_j can be obtained directly as the time histories or frequency spectra. Specifically, it is the peak acceleration of the monitoring point under seismic excitation, as shown in Table 3.

In general, when $r \geq 0.9$, the impact of boundary effects on model tests is considered negligible (Wang et al., 2023b; Hu et al., 2021). In addition, a smaller value of μ indicates that x and y are closer, and when $\mu = 0$, it signifies that the boundary and the central point's respond identically. It can be seen from Table 4 that the variation ranges of r and μ in this experiment are 0.95–0.99 and 0.02–0.2, respectively, indicating that the boundary effects can be ignored. As peak acceleration increases, the values of r decrease and the values of μ increases, indicating that the boundary effects become more pronounced with higher earthquake intensity. Moreover, it is evident that boundary effects vary under different seismic excitation cases. The boundary effects under Wolong seismic motion are more pronounced than those under Menyuan seismic motion, which may be attributed to differences in frequency content and the development of nonlinear behavior in the model soil. However, the trend in these changes is consistent under both types of seismic excitations. The uniformity of dynamic responses across various measurement points along the boundaries under different seismic excitations suggests that the fault container satisfies the experimental boundary conditions. Therefore, the novel fault container is deemed suitable for simulating the boundary conditions of a real site accurately.

4.5. Validation of seismic motion and fault coupling effects

4.5.1. Acceleration amplification along depth

Acceleration data recorded from the free-field test (A11, A31, A51) were utilized to investigate the free-field amplification effect of the model soil under various seismic excitation scenarios. Fig. 16a–c illustrates the peak acceleration amplification with depth across three different excitation intensities. The amplification effect under Wolong seismic motion was found to exceed that under Menyuan seismic motion at all three intensity levels, as indicated by the amplification coefficients. This greater amplification under Wolong seismic motion is attributed to the closer alignment between its base frequency and the base frequency of the model soil, resulting in a more pronounced acceleration response. Additionally, it is generally observed that surface amplification effects decrease with increasing input peak acceleration (Yang et al., 2021; Xin et al., 2024a). However, in this study, the elevation amplification factor initially decreases and then increases with increasing peak acceleration, reflecting the nonlinearity exhibited by the model soil under seismic loading.

Using acceleration data recorded from the free-field test (A14, A34, A54), the dynamic response characteristics of the model soil in the hanging wall and footwall sections of the fault are also investigated. Fig. 16d shows the peak acceleration amplification with depth in the hanging wall and footwall sections under 0.4 *g* Menyuan seismic motion. The amplification factor in the hanging wall section is significantly greater than that in the footwall section, aligning with the previous findings that the response in the hanging wall section in test group 1 is stronger than in the footwall section. Furthermore, when comparing Fig. 16b with Fig. 16d, an increase in the elevation amplification effect is observed post-dislocation. This change is attributed to fault dislocation, which causes localized damage to the model soil, while the majority of the soil in other regions transitions into the plastic stage. This transition leads to a reduction in soil stiffness, resulting in increased nonlinearity and an enhanced deformation capacity under seismic loading.

4.5.2. Time-frequency domain analysis before and after dislocation

In the shaking table tests, the frequency domain analysis of the seismic motions in the free-field model before and after fault dislocation is conducted to evaluate the impact of fault dislocation on seismic wave propagation characteristics. The Fourier spectrum changes at the boundary monitoring points of the hanging wall and footwall sections under 0.4 *g* Menyuan seismic motion, before and after dislocation, are compared as shown in Fig. 17.

From Fig. 17a and b, it can be observed that, in the free-field test, the main frequency of the Menyuan seismic motion at the bottom of the hanging wall and footwall of the fault changes minimally before and after dislocation, which can be considered negligible. This stability results from their relatively stable positional characteristics with respect to the fault dislocation, which causes minimal changes in the propagation path and less impact from reflection and refraction. In the central region of the free-field, Fig. 17c and

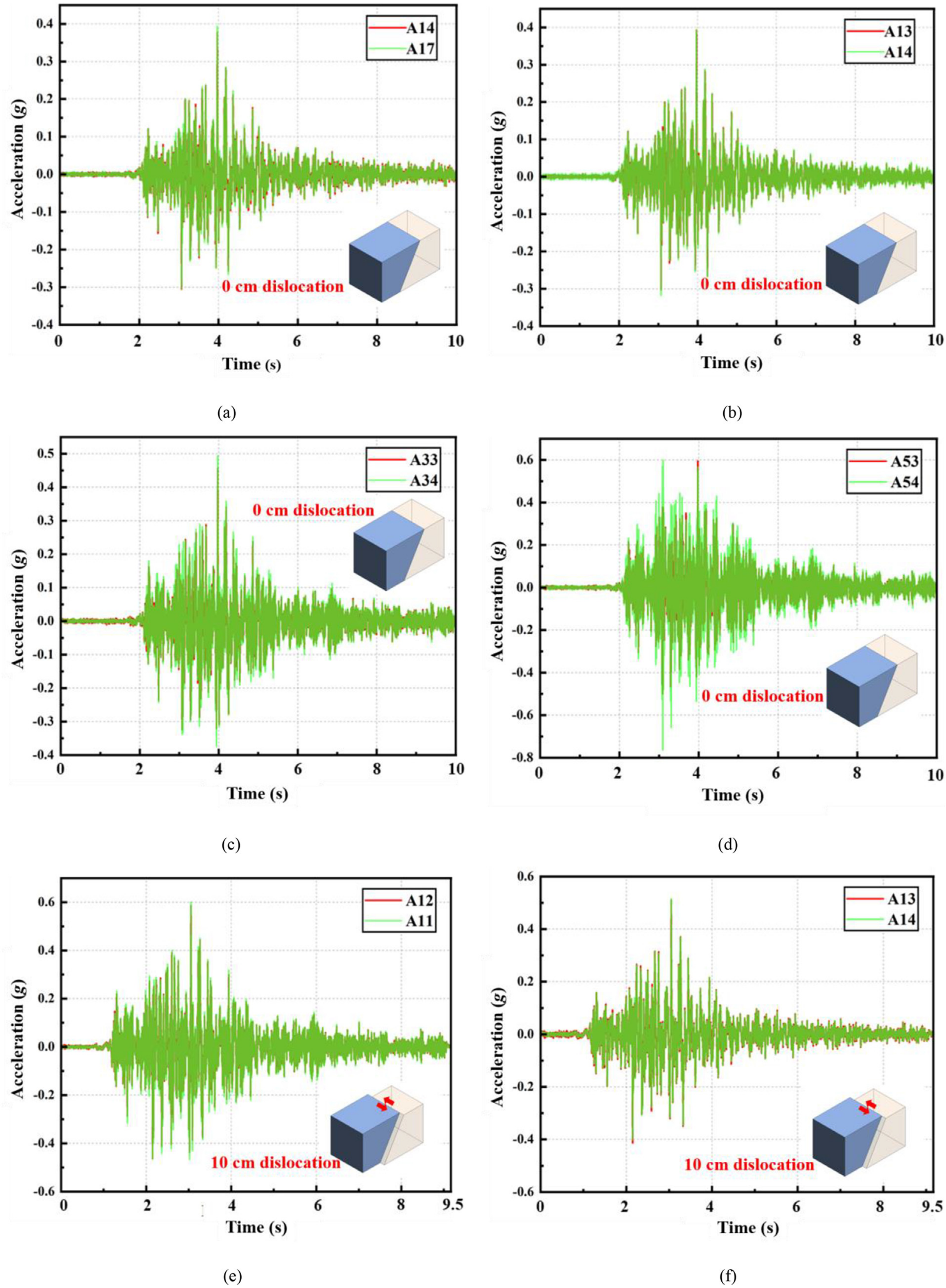

Fig. 15. Comparison chart of acceleration time history curves at measurement points: (a) Lateral boundary; (b) Longitudinal boundary; (c) Central boundary; (d) Top boundary; (e) Hanging wall boundary; and (f) Footwall boundary.

Table 3
Peak acceleration at measurement points A34 and A33 in the shaking table tests.

Monitoring point	Imposed seismic motion	Input peak acceleration		
		0.2	0.4	1.0
A34	Menyuan	0.247	0.456	1.186
	Wolong	0.227	0.464	1.351
A33	Menyuan	0.253	0.493	1.218
	Wolong	0.234	0.504	1.416

Table 4
Correlation coefficient and 2-norm deviation at measurement points in the shaking table tests.

Input peak acceleration	r		μ	
	Menyuan	Wolong	Menyuan	Wolong
0.2	0.983	0.991	0.024	0.031
0.4	0.972	0.982	0.081	0.086
1.0	0.955	0.961	0.139	0.163

d clearly shows that the spectral characteristics of the Menyuan seismic motion in the hanging wall and footwall differ post-dislocation. For the footwall section, the main frequency remains around 7.3 Hz both before and after dislocation, showing no significant change. In contrast, in the hanging wall section, the main frequency of the Menyuan seismic motion decreases significantly from 7.299 Hz to 2.262 Hz before and after dislocation. This notable reduction in the main frequency of the hanging wall extends to the free-field surface (Fig. 17e and f). Specifically, the main frequency of the seismic motions on the hanging wall surface decreases following fault dislocation, whereas the main frequency on the footwall surface remains relatively stable. This change is primarily attributed to the fault dislocation in the hanging wall, which leads to soil damage and amplifies the reflection and refraction effects of the seismic waves. These effects alter the propagation path and frequency components of the waveform, resulting in a reduction in the main frequency. In contrast, the impact of dislocation on the footwall section is less pronounced, leading to minimal changes in the main frequency of the seismic motions. This phenomenon aligns with the observation from Wenchuan earthquake, where the damage to the hanging wall of the Longmenshan fault zone was significantly greater than that to the footwall, consistent with theoretical expectations (Yu et al., 2016). This analysis further demonstrates that the container effectively simulates the coupling effects of fault dislocation and near-fault pulse seismic motion.

To verify the effectiveness of the coupling effect between the

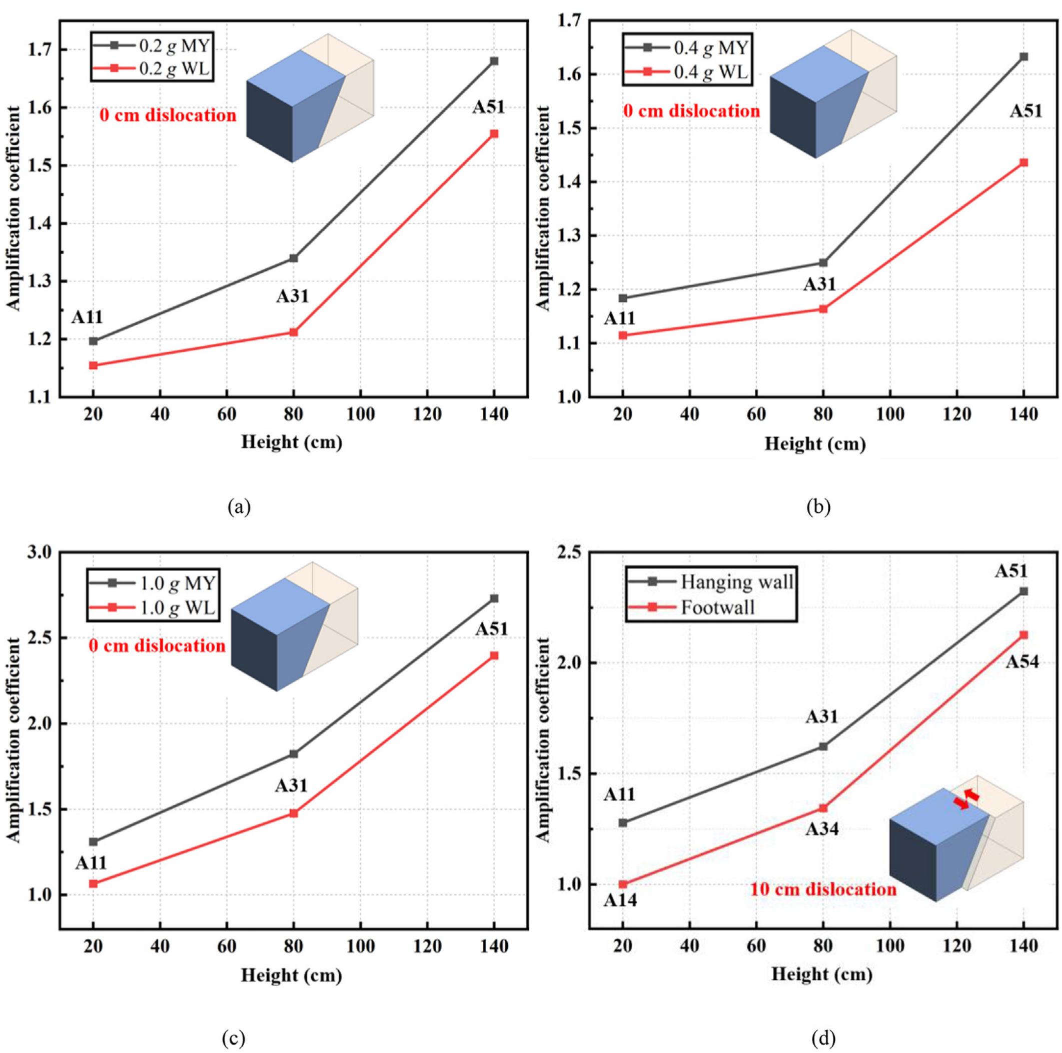

Fig. 16. Comparison chart of amplification factors for different peak accelerations and fault dislocation: (a) 0.2 g Comparison of amplification factors; (b) 0.4 g Comparison of amplification factors; (c) 1.0 g Comparison of amplification factors; and (d) Comparison of amplification factors for a 10 cm fault dislocation at 0.4 g acceleration.

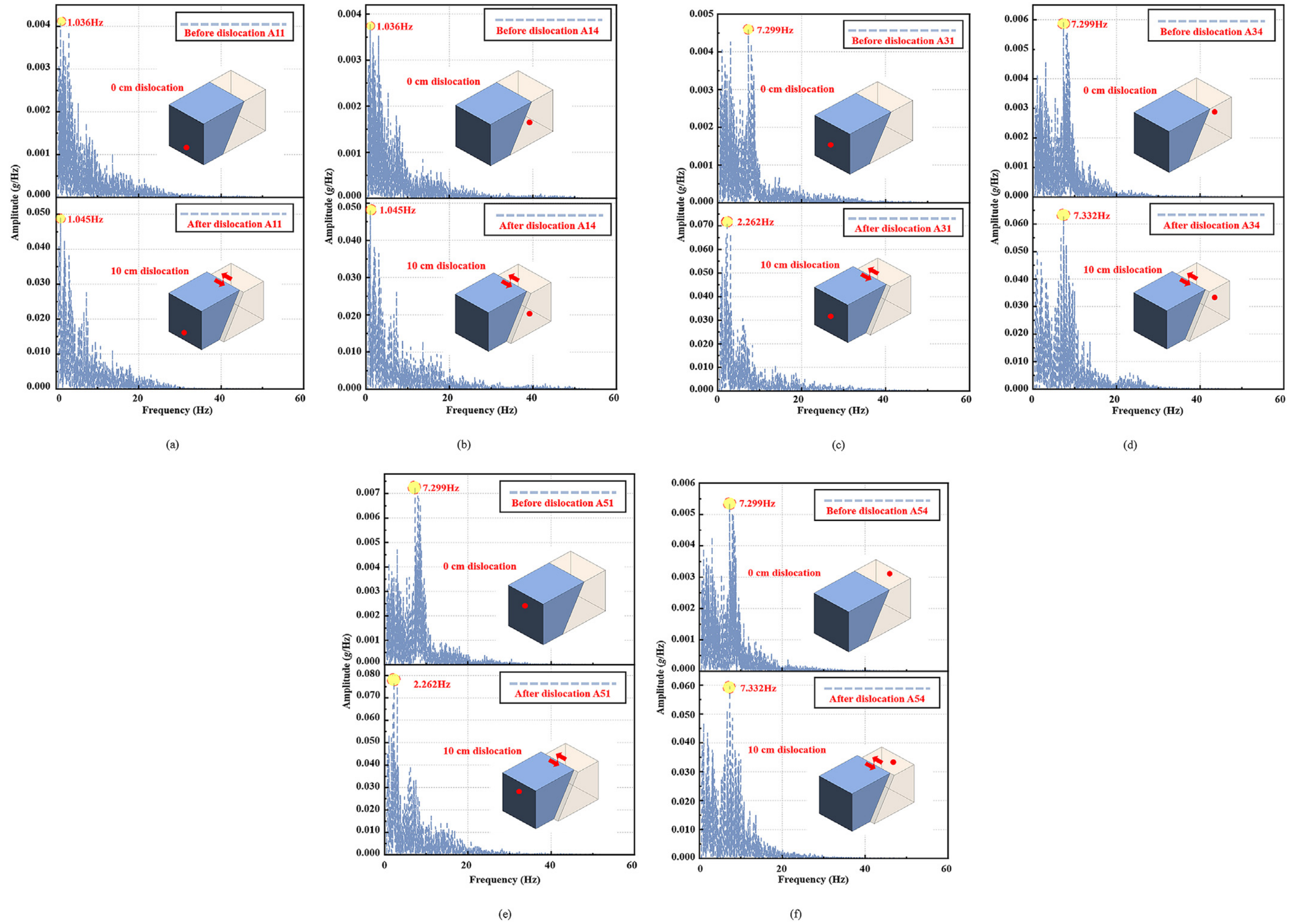

Fig. 17. Comparison chart of Fourier spectra at different locations: (a) Fourier spectrum at A11; (b) Fourier spectrum at A14; (c) Fourier spectrum at A31; (d) Fourier spectrum at A34; (e) Fourier spectrum at A51; and (f) Fourier spectrum at A54.

fault and the seismic motion simulated by the container. 0.4 *g* Menyuan seismic motion was selected to study the influence of fault dislocation on acceleration response at fault, and the acceleration time history curves of different monitoring positions at fault are compared and analyzed, as shown in Fig. 18. According to Fig. 18a–c and e, before fault dislocation occurred, the acceleration time-history curves near the fault at the same elevation were similar, which indicates that the container as a whole has a satisfactory dynamic carrying capacity and integrity under the condition of no dislocation, and can truly reflect the corresponding law of the real dynamic force of seismic motion in the free field. According to Fig. 18b–d and f, the acceleration time history curve is different after the fault dislocation of 10 cm, specifically, the acceleration response of the hanging wall is greater than that of the footwall, which is consistent with the conclusion obtained in Section 4.4 of this study. In addition, by comparing Fig. 18a and b, it can be found that the acceleration response after 10 cm fault dislocation is greater than that before fault dislocation. This indicates that the fault dislocation will intensify the acceleration response at the fault, and the fault dislocation will release more energy. It is further demonstrated that the model container can simulate the coupling effect of fault and seismic motion.

In addition, the Daliang tunnel serves as an example in this study, and the model materials at both ends of the model test are selected for mechanical properties testing. Based on the geometric dimensions of the prototype tunnel and the specifications of the shaking table, the geometric similarity ratio is determined to be 1:30. Geometric length, density, and elastic modulus were selected as control parameters, which were then used to derive the similarity relationships for key parameters. The physical and mechanical properties at the fault location, following fault dislocation and surrounding rock movement, are summarized in Table 5. As shown in Table 5, after the occurrence of fault dislocation, the measured values at both the fault and the surrounding rock at each end conform to the order of magnitude calculated using the similarity relation. This indicates that the dynamic characteristics of the soil at the fault location can be accurately simulated.

Moreover, the seismic damage phenomenon on the surface of the free field shaking table test further verifies the difference between the hanging wall and footwall caused by fault dislocation, as shown in Fig. 19. Under the same peak acceleration excitation conditions, the damage observed in the hanging wall prior to dislocation is greater than that in the footwall. The primary seismic damage manifests as small cracks, with the “hanging wall effect” remaining relatively subtle. This can be attributed to the container holding the hanging wall and footwall together as an integral rigid structure through high-strength bolts before fault dislocation. Following the coupled action of a 10 cm dislocation and seismic motion, the surface cracks in the soil of the hanging wall and footwall become more pronounced, resulting in the appearance of significant wide cracks. This enhancement of the “hanging wall effect” is clearly evident. These observations indicate that the

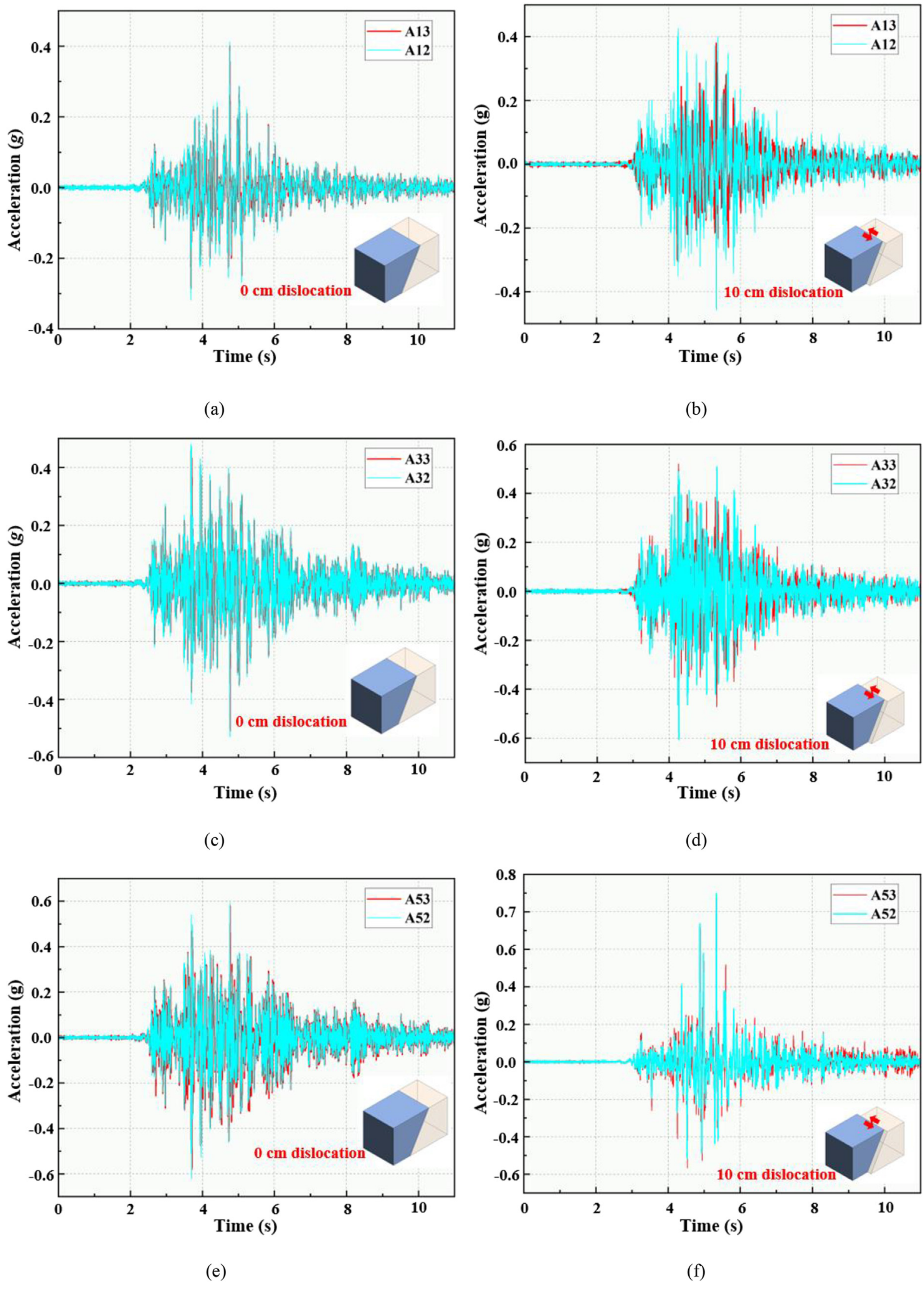

Fig. 18. Acceleration time history curve at the fault before and after the dislocation at the same measuring point: (a) no dislocation for bottom; (b) 10 cm dislocation for bottom; (c) no dislocation for central; (d) 10 cm dislocation for central; (e) no dislocation for top; and (f) 10 cm dislocation for top.

Table 5
Physical and mechanical parameters of surrounding rock and fault.

Item		Density (g/cm^3)	Elasticity modulus (MPa)	Poisson's ratio	Frictional angle (°)	Cohesion force (KPa)
Surrounding Rock	Prototype value	1.8–2.0	1300–2000	0.35–0.39	22–27	120–200
	Require value	1.4–1.5	33.3–51.3	0.35–0.39	22–27	3.1–5.1
	Measured value	1.49	41.1	0.35	25.3	3.2
Fault	Prototype value	1.7–1.8	1000–1300	0.39–0.45	20–22	50–120
	Require value	1.3–1.4	25.6–33.3	0.39–0.45	20–22	1.3–3.1
	Measured value	1.37	28.2	0.42	20.1	1.5

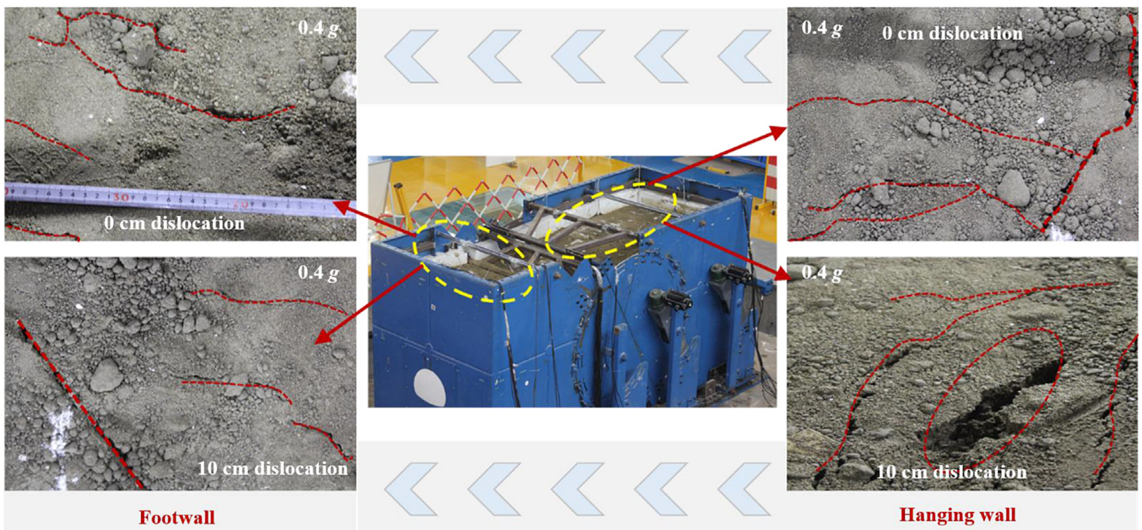

Fig. 19. Comparison of hanging wall and footwall seismic damage phenomena before and after 0.4 *g* MY seismic motion dislocation.

coupling of fault dislocation and seismic motion can result in greater damage to the model soil, while also creating more distinct differences in the failure phenomena of the hanging wall and footwall. This phenomenon aligns with theoretical expectations and further validates that the container can effectively simulate the coupling effect of seismogenic faults.

5. Analysis of numerical simulation results

5.1. Finite element model building

To validate the performance of the fault container, the finite element software ABAQUS was utilized to analyze the test equipment. The inclination adjustment device, along with the hanging wall and footwall, is connected using high-strength bolts to form the integrated frame of the container. This assembly is therefore modeled as a single entity in the analysis. The motors used in the model tests simulate fault strike-slip, however, their impact on the container's strength is not being considered. The shearing frame structure, welded between the container and both the hanging wall and footwall cabinets, was modeled using a combination of finite elements. Specifically, 4-node shell elements (S4R) were used for shearing frame component, and 8-node solid elements (C3D8R) were applied to the hanging wall and footwall cabinets. Additionally, 2-node beam elements (B31) were selected for the support beam rods within the model to accurately represent their linear, load-bearing characteristics. These modeling details are illustrated in Fig. 20.

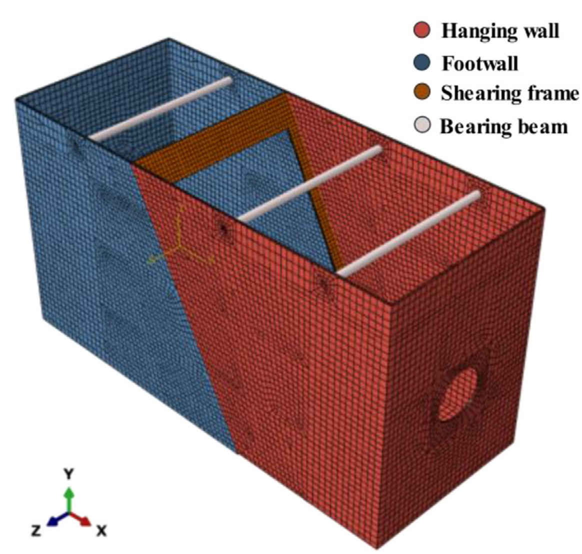

Fig. 20. Numerical simulation model.

5.1.1. Physical and mechanical parameters of materials are introduced

In the numerical simulation, the container was simulated using an ideal elastic-plastic constitutive model, as shown in Fig. 21. The steel material of the container is described in Section 2.2, and the material parameters are listed in Table 6.

5.1.2. Boundary conditions and contact settings

The hanging wall and footwall of the fault shear frame were placed in face-to-face contact to facilitate effective load transfer under stress. The sidewalls of both the hanging wall and footwall

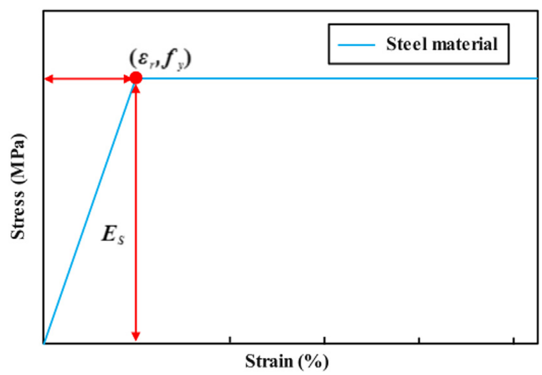

Fig. 21. Elastic-plastic constitutive model of steel.

Table 6
Physical and mechanical parameters of materials.

Material	Density (kg/m^3)	Young's modulus (GPa)	Poisson's ratio
Steel	7850	206	0.3

were constrained to the bottom plate using bonding constraints, which restrict movement and deformation of the frame relative to the bottom plate. Coupling constraints were employed between the beams and sidewalls of the hanging wall and footwall to simulate their shared load characteristics and ensure accurate load transfer under vibration or stress. Additionally, bonding constraints were applied between the shear frame and the fault section to prevent relative sliding under load. Vertical constraints were applied to the entire container to fix the model bottom plate, reflecting its attachment to the shaking table during the tests. This setup prevent irregular deformation and vertical displacement of the bottom plate, ensuring the stability and integrity of the simulation environment.

5.2. Analysis of container self-oscillation frequency

Fig. 22 shows that the natural frequency of the container, as determined by the numerical simulation, is 24.23 Hz. This frequency closely aligns with the shaking table test result of 23.74 Hz, with the difference falling within a 5% error margin. This slight discrepancy confirms the accuracy and reliability of the numerical simulation, demonstrating its effectiveness in capturing the key characteristics of structural vibrations.

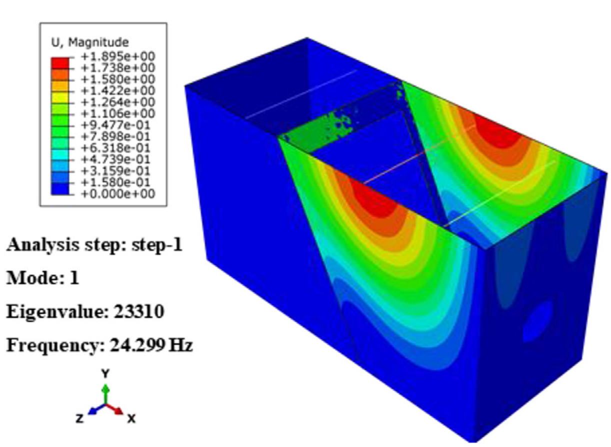

Fig. 22. The first-order natural frequency and vibration mode diagram of the container.

Additionally, in tunnel engineering subjected to strong seismic actions triggered by strike-slip faulting, the dynamic response of the hanging wall typically exceeds that of the footwall (Wen et al., 2021). In the shaking table tests, the hanging wall of the container functions as the active block, leading to relatively weaker constraints on it. Consequently, in the numerical simulation, the displacement response of the hanging wall is observed to be greater than that of the footwall, with a maximum displacement recorded at 1.90 mm under the first modal condition. This pattern is consistent with the acceleration response observed in the shaking table tests. Overall, the container exhibits minimal displacement under the natural frequency condition and maintains robust structural integrity.

5.2.1. Modal analysis under different dislocation patterns

Given the reliability of the numerical simulation, a further in-depth analysis was conducted on the modal characteristics of the container under different dislocation patterns. Fig. 23a–c displays the first-order natural frequency displacement cloud maps and mode shapes of the container under horizontal, vertical, and combined horizontal-vertical dislocation of 10 cm, respectively. By adjusting the dislocation parameters, variations in different vibration modes were observed. This approach facilitates a more comprehensive understanding of the structural vibration characteristics.

From Fig. 23, it can be seen that the first-order natural frequency of the container exhibits minimal variation across different dislocation cases, and the response of the hanging wall is greater than that of the footwall, consistent with the experimental observations. Fig. 23a and b reveals notable changes in the mode shapes for vertical and horizontal dislocations, with the maximum displacement increasing from 1.896 mm to 2.240 mm. Fig. 23b and c indicates how vertical dislocation particularly affects the mode shape of the container. This effect is attributed to the reduced contact area between the hanging wall and footwall due to vertical dislocation, which significantly weakens the constraints of the hanging wall shear frame, resulting in increased displacement at this location, although the increase is not substantial. These observations demonstrate that the container has a certain degree of adaptability to different dislocation modes, maintaining stable vibration modes and showcasing its adaptability and reliability under various conditions. By comparing Figs. 22 and 23a, it is observed that the impact of increased displacement due to greater dislocation is not significant. This suggests that the container exhibits robustness and integrity even when subjected to changes in dislocation conditions, maintaining stable vibration modes.

5.2.2. Harmonic response analysis

To verify the resonance conditions of the fault container at specific frequencies, a sinusoidal sweep test was conducted, covering a frequency range from 0 to 60 Hz. This test was designed to analyze the steady-state response of the container under periodic excitation and to identify potential structural resonance issues that may be induced by seismic motions at various frequencies.

As shown in Fig. 24a, the structural displacement response of the hanging wall is higher than that of the footwall, aligning with the test results. This greater displacement is primarily because the hanging wall acts as the active plate, which possesses greater degrees of freedom and undergoing slight relative displacements at the contact area with the footwall during seismic activity. The frequency-displacement curve analysis at point B of the container, shown in Fig. 24b, indicates that within the 0–60 Hz sweep frequency range, the structure reaches its maximum displacement of 0.56 mm at 25.23 Hz. This peak displacement falls within a 5% error

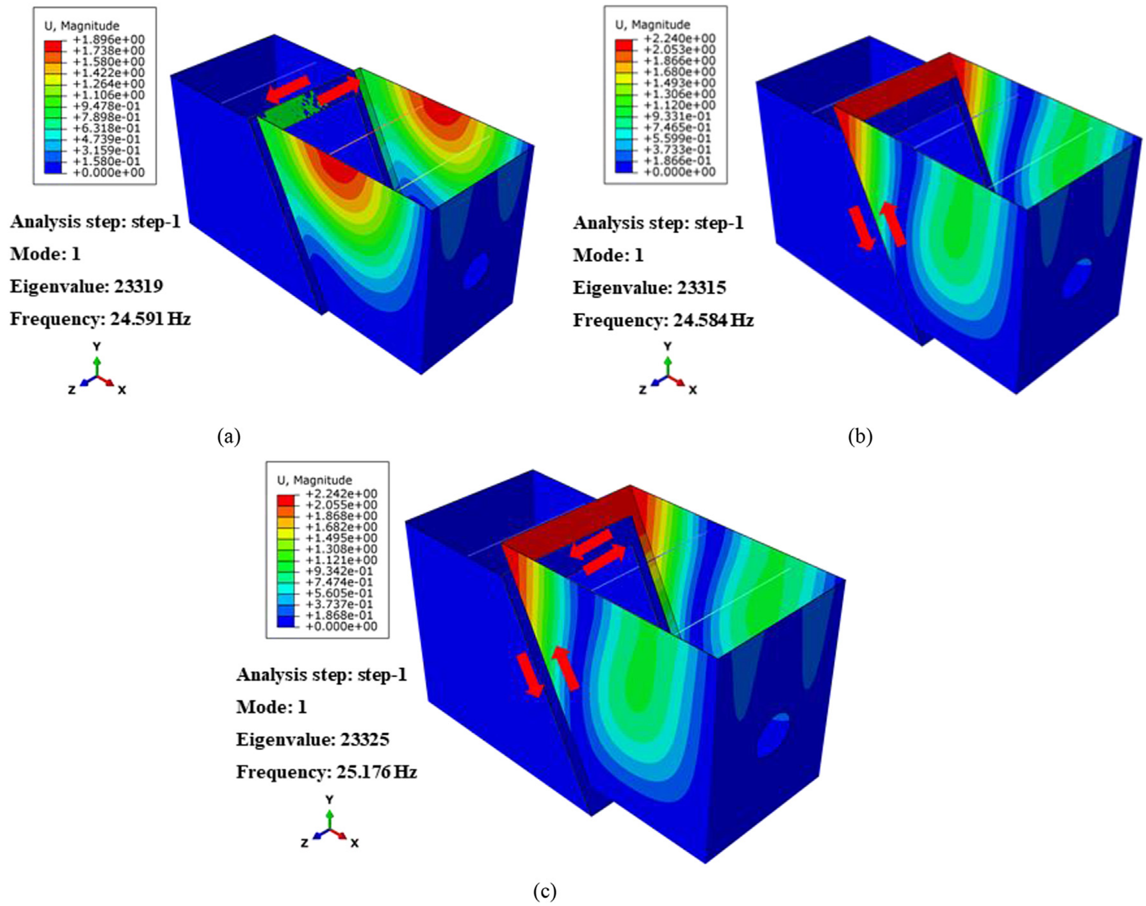

Fig. 23. The first-order natural frequency and vibration mode diagram of the container under different stagger distances: (a) 10 cm horizontal dislocation; (b) 10 cm vertical dislocation; and (c) 10 cm horizontal and vertical dislocation.

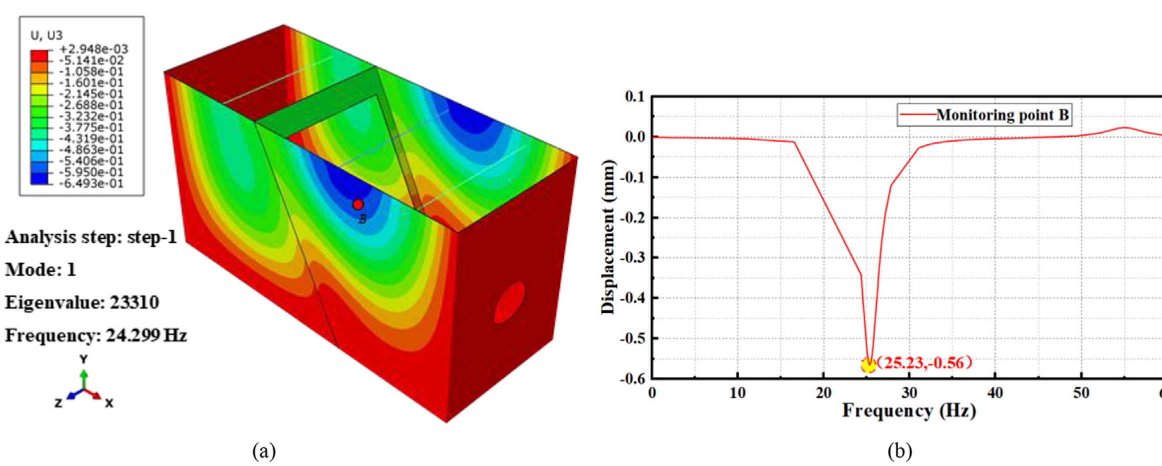

Fig. 24. Harmonic response analysis modal characteristics: (a) Harmonic response displacement cloud diagram; and (b) Harmonic response frequency-displacement curve.

margin compared to the model test data, affirming that the container resonates at this frequency. Despite this resonance, the container maintains good stability and structural integrity under both low- and high-frequency seismic excitations.

5.2.3. Random response analysis

Random vibration analysis is a spectral analysis method that leverages modal analysis results combined with known spectra to calculate the structural response. This technique is predominantly utilized to assess the dynamic response of structures subjected to random or time-varying loads (Zhang et al., 2022). The purpose of employing random vibration analysis in this study was to explore the uncertainty and variability in the behavior of the fault container during seismic activities. Simulations of random vibrations under various seismic excitations were conducted to gain a comprehensive understanding of the container's dynamic response under such conditions. For this analysis, the white noise recorded during the shaking table tests served as the input for Fourier transform analysis. Subsequently, the power spectral density (PSD) was computed, providing a detailed view of the energy distribution across frequency bands. The resulting PSD curve is illustrated in Fig. 25. This curve helps identify the frequencies at which the container is most responsive to seismic inputs, aiding in predicting and mitigating potential issues in real-world applications.

Fig. 26 shows the random vibration acceleration cloud map obtained from the PSD curves input into the finite element software. The map reveals that the container exhibits a "hanging wall effect" and an "elevation amplification effect", consistent with the observations made in experimental settings. The "hanging wall effect" refers to the enhanced seismic response experienced by structures located on the hanging wall of a fault during an earthquake (Cui et al., 2022a; Fei et al., 2024). Specifically, in the region above the fault, particularly near the fault surface, the dislocation has a pronounced effect, leading to a significant increase in the displacement, strain, and acceleration of the hanging wall (Zhong et al., 2020; Gou et al., 2024). This consistency confirms the accuracy of the simulation relative to actual dynamic behavior. Further analysis involving the extraction of the acceleration-frequency curve at point C of the container (shown in Fig. 27), indicates that the acceleration amplitude occurs at a frequency of 25.23 Hz. This frequency corresponds closely with the model tests and harmonic response analysis. The observed acceleration responses at both high and low frequencies are attributed to resonance phenomena, occurring when the seismic excitation frequency aligns with other-order natural frequencies of the container. Despite these resonance effects, the significant differences between these responses and the primary frequency acceleration response of the container suggest that their impact on the overall experimental outcomes is minimal. This observation demonstrates that the container maintains robust stability and structural integrity under random vibration conditions.

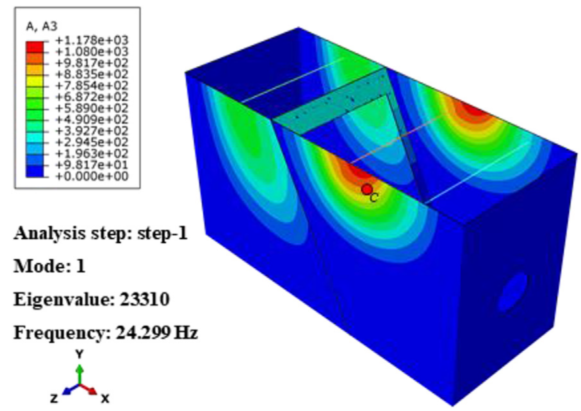

Fig. 26. Random response first-order natural frequency and vibration mode diagram.

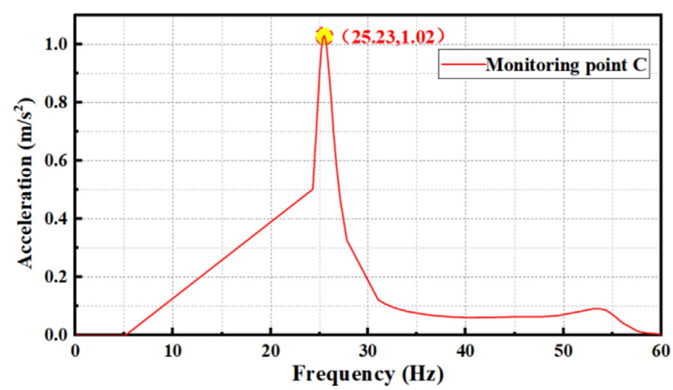

Fig. 27. Random response frequency-acceleration curve.

6. Discussion

This study comprehensively investigated the modal characteristics and dynamic response features of the fault container through extensive large-scale shaking table tests and detailed numerical simulations. The analysis of these tests demonstrated that the fault container exhibited commendable stability and structural integrity under the influence of strong seismic actions, particularly those triggered by strike-slip active faults. To delve deeper into the modal characteristics of the fault container and to enhance the accuracy of the test results, Siemens' hammer signal processing technology was employed. This method facilitated an in-depth analysis of the modal characteristics, providing a clearer understanding of its dynamic behavior under various conditions. To accurately capture the structural modal characteristics, accelerometers were placed on different surfaces of the container. These surfaces, labeled as A, B, C, and D, are illustrated in Fig. 28. This placement was designed to maximize data acquisition and enhance the precision of the modal analysis.

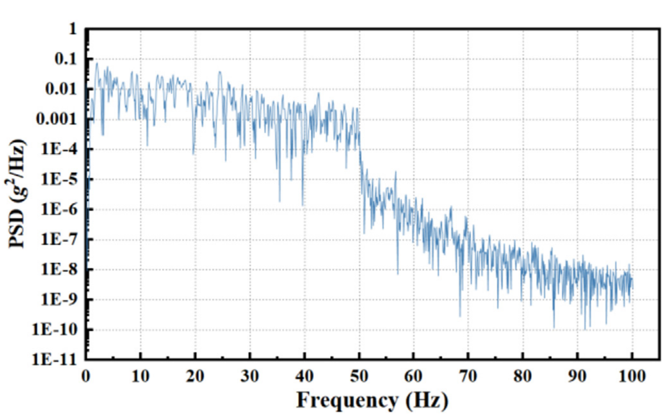

Fig. 25. The power spectrum curve.

Digital signal processing techniques were used to sample the Frequency Response Function (FRF) derived from the model. The test employed the Least Squares Complex Exponential method (LSCE) to estimate the modal frequencies and damping factors of the container. The LSCE method was employed in the test to estimate the modal frequencies and damping factors of the container modes. The least squares error associated with the solution of Eq. (3) was evaluated by analyzing the convergence with respect to the number of assumed modes (Chung and Sernaker, 1994).

$$\begin{pmatrix} r_{1,1} & r_{1,2} & \cdots & r_{1,2N} \\ \bullet & r_{2,2} & \cdots & r_{2,2N} \\ \vdots & \vdots & \vdots & \vdots \\ \bullet & \bullet & \bullet & r_{2N,2N} \end{pmatrix} \begin{Bmatrix} a_1 \\ a_2 \\ \vdots \\ a_N \end{Bmatrix} = \begin{Bmatrix} -r_{1,0} \\ -r_{2,0} \\ \vdots \\ -r_{2N,0} \end{Bmatrix} \tag{3}$$

where r is the generalized Hankel matrix, and a is the autoregressive coefficient.

For this reason, when initially establishing an equation such as Eq. (3), it is assumed that a sufficiently large number of modes, N, is present. Specifically, a subset of this equation used to solve the coefficient of the model addresses the scenario where only a single mode is expressed, as demonstrated in Eq. (4).

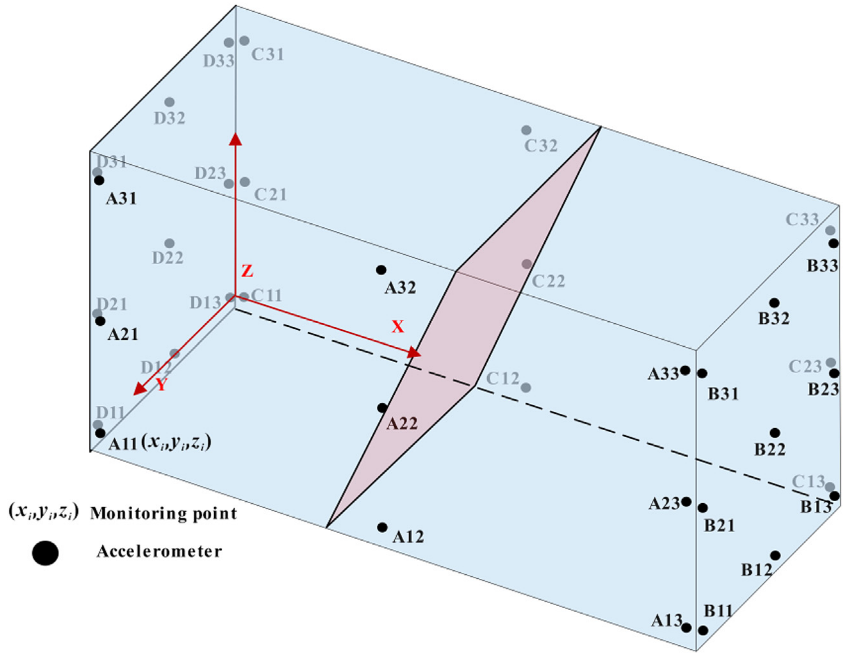

Fig. 28. Accelerometer arrangement of hammer test.

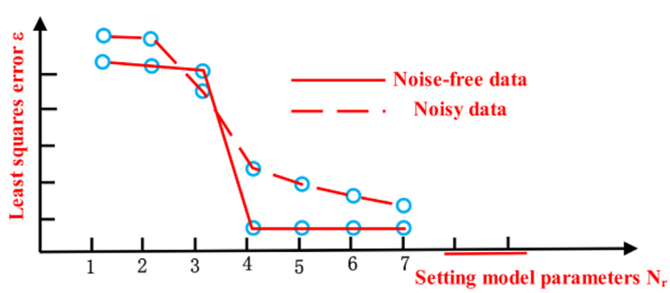

Fig. 29. Least square error diagram.

$$\begin{pmatrix} r_{1,1} & r_{1,2} \\ \cdot & r_{2,2} \end{pmatrix} \begin{Bmatrix} a_1 \\ a_2 \end{Bmatrix} = \begin{Bmatrix} -r_{1,0} \\ -r_{2,0} \end{Bmatrix} \tag{4}$$

The corresponding least squares error is denoted by ε_1. When the data is assumed to contain two modes, the subset to be solved is shown in Eq. (5).

$$\begin{pmatrix} r_{1,1} & r_{1,2} & r_{1,3} & r_{1,4} \\ \cdot & r_{2,2} & r_{2,3} & r_{2,4} \\ \cdot & \cdot & r_{3,3} & r_{3,4} \\ \cdot & \cdot & \cdot & r_{4,4} \end{pmatrix} \begin{Bmatrix} a_1 \\ a_2 \\ a_3 \\ a_4 \end{Bmatrix} = \begin{Bmatrix} -r_{1,0} \\ -r_{2,0} \\ -r_{3,0} \\ -r_{4,0} \end{Bmatrix} \tag{5}$$

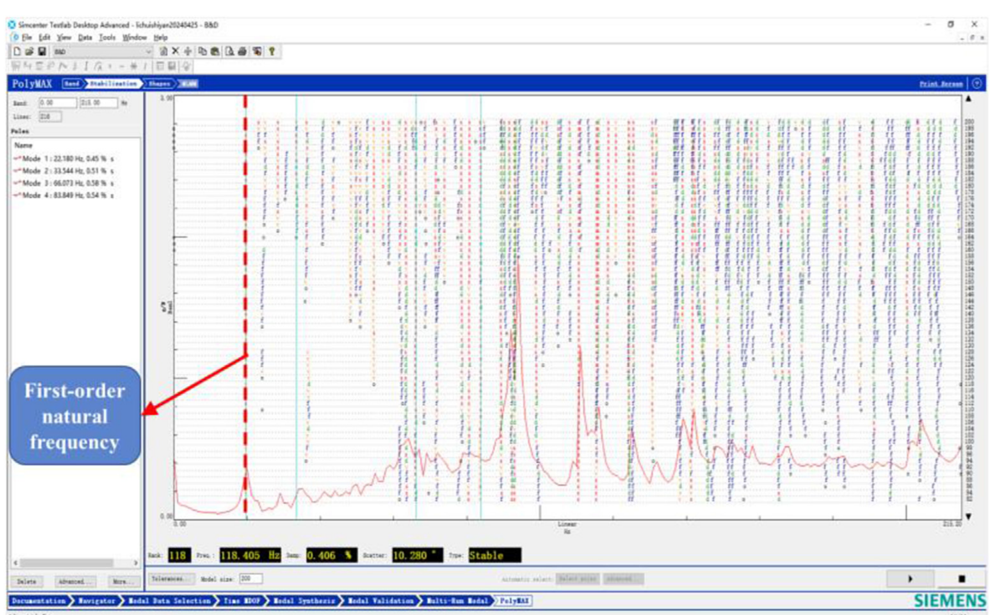

Fig. 30. Container steady state diagram.

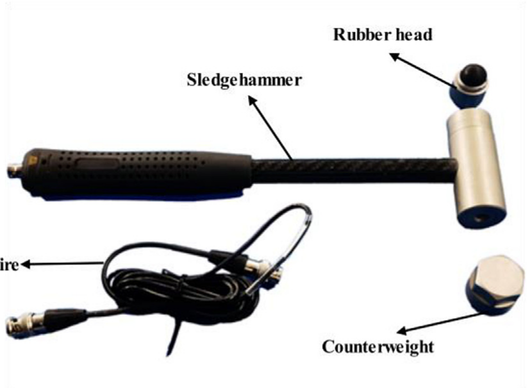

Fig. 31. Force hammer sensor.

Similarly, when the number of assumed modes in the model accurately reflects the actual number of modes present in the data, the corresponding least squares error ε_2 is expected to be significantly smaller compared to the error observed when fewer modes are assumed (Feng, 2013).

The variation of the least squares error with the increasing number of assumed modes is plotted to create the least squares error plot, as shown in Fig. 29.

The optimal number of modes was determined by comparing the estimated frequencies and damping factors across models with varying numbers of assumed modes. Ideally, these estimated frequencies and damping factors should remain relatively stable, even as the number of assumed modes changes. A steady-state plot is used to illustrate how modal frequencies and damping factors vary with an increasing number of assumed modes. By analyzing this steady-state plot (Fig. 30), the optimal number of modes can be identified. This optimal point is where further increases in the number of modes no longer significantly refine the estimates.

Tapping tests were conducted using a force hammer sensor (refer to Fig. 31) at the locations of the accelerometers to acquire the relevant test data. The specific parameters of these tests are detailed in Table 7. The collected data were processed and analyzed, and then compared with results from shaking table tests and numerical simulations. This comparison validated the fault container's modal characteristics and dynamic response features, confirming the applicability and accuracy of the test methods used.

As shown in Fig. 32, the force hammer test results indicate that the first-order natural frequency of the fault container is 22.18 Hz with a damping ratio of 0.45%. When these results are compared with those from shaking table tests and numerical simulations, they are found to be in good agreement. Additionally, the test mode shapes demonstrate the container's excellent overall integrity and adaptability.

7. Conclusions

The modal characteristics of the fault container were effectively determined through shaking table tests, numerical simulations, and force hammer testing. The dynamic response features of the container from both the first and second group of experiments were analyzed. Additionally, the container's effectiveness in simulating the coupling effects between the fault dislocation and seismic excitation was validated. The results from the shaking table tests, numerical simulations conducted under various scenarios, and hammer test modal characteristics were found to be consistent, affirming the reliability of the methodologies employed. The specific conclusions are as follows:

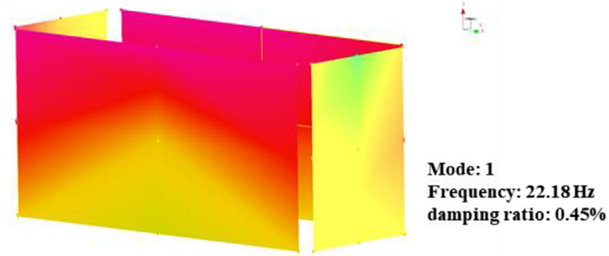

Fig. 32. The first-order natural frequency and vibration mode diagram of hammer test.

(1) The natural frequencies of the container and the model soil, measured using the scanning frequency method, are 23.74 Hz and 6.355 Hz, respectively. The significant difference between these frequencies ensures that resonance between the container and the model soil is unlikely. Additionally, the natural frequency of the model container deviates significantly from those commonly used in similar studies, further demonstrating the broad applicability of the container. The consistency of response signals at the same measurement points in the container across various dislocations is satisfactory, and the similarity of waveforms at different points confirms the design's integrity and reasonableness. The test results from group 1 revealed that the amplification effect of the Wolong seismic motion is greater than that of the Menyuan seismic motion. Additionally, for the same seismic motion, the amplification effect becomes more pronounced with increasing acceleration amplitudes.

(2) Test group 2 quantitatively analyzed the impact of boundary effects on soil seismic responses using 2-norm deviations, cumulative moment correlation coefficients, acceleration time history waveforms, and Fourier spectral characteristics. The analysis reveals that the container boundaries have minimal impact on the soil's seismic response. The Wolong seismic motion consistently shows a greater amplification factor compared to the Menyuan seismic motion. Additionally, the Fourier spectra of seismic waves before and after dislocation excitation confirmed that the container effectively simulates the coupling effect between fault dislocation and seismic motion, thereby validating the container's reasonableness and applicability.

(3) Numerical simulation results indicated that the first-order natural frequency of the container remains relatively stable across various dislocation scenarios. Significant changes in the vibration modes are observed between vertical and horizontal dislocations, with vertical dislocation

Table 7
Main parameters of force hammer sensor.

Axial sensitivity ((23 ± 5) °C)	Measuring range	Maximum lateral sensitivity	Maximum output signal	Installation resonance frequency	Polarity (acceleration direction from the bottom to the sensor)	Resolution
1 mV/N	0-60 KN	0.05 mV/N	5 V	>22 kHz	Positive direction	<0.001 N

predominantly influencing the container's vibration modes. The increase in dislocation distance does not significantly affect displacement, suggesting that the container demonstrates considerable robustness and structural integrity under varying dislocation conditions, thereby maintaining stable fundamental vibration modes.

(4) Under specific frequency or random seismic excitations, the response of the hanging wall of the container is consistently higher than that of the footwall. Within the frequency sweep range of 0-60 Hz, maximum displacement-acceleration occurs at the natural frequency of the container due to the resonance phenomena. The displacement-acceleration contour maps reveal pronounced “hanging wall effects” and “elevation amplification effects” within the container. Further analysis of the frequency-displacement-acceleration curves, alongside hammer test results, substantiates the accuracy of the natural frequency measurements of the container. The container also demonstrates robust adaptability and maintains integrity under both low-frequency and high-frequency seismic excitations.

(5) In future research, this container will be utilized to investigate various coupling mechanisms between different active fault strike-slip behaviors and seismic motions. Additionally, the dynamic response characteristics and anti-seismic mechanisms of crossing-fault tunnels under various anti-seismic measures will be examined, with the aim of proposing partitioned resilience repair strategies for high-speed railway tunnel linings following earthquakes. Furthermore, shaking table tests are employed to study and validate the instability criterion and control method of three seismic resilience-enhancing schemes, which focus on enhancing the ductility of structures, reducing seismic energy transformation, and localizing seismic damage to facilitate easier repairs, which provides a theoretical basis for seismic fortification of tunnel engineering.

CRediT authorship contribution statement

Wenkai Feng: Writing – review & editing, Funding acquisition. **Lianjie Yang:** Writing – original draft, Software, Data curation. **Chunlei Xin:** Supervision, Methodology, Funding acquisition. **Zhao Wang:** Writing – review & editing, Formal analysis. **Xinyuan Yu:** Visualization. **Yixin Shuai:** Software. **Yuxin Tian:** Validation.

Data availability statement

The original data supporting the conclusions of this article will be made available by the authors, without undue reservation.

Declaration of competing interest

The authors declare that they have no known competing financial interests or personal relationships that could have appeared to influence the work reported in this paper.

Acknowledgments

This research was supported by the National Natural Science Foundation of China (Grant Nos. 52108361 and 41977252), the Sichuan Science and Technology Program of China (Grant Nos. 2024ZYD0154 and 2024NSFSC0159), and the State Key Laboratory of Geohazard Prevention and Geoenvironment Protection Independent Research Project (Grant Nos. SKLGP2022Z015 and SKLGP2020Z001). All authors acknowledge the anonymous reviewers for their comments.

References

Cengiz, C., Guler, E., 2020. A laminar container apparatus for 1 g testing of granular columns embedded in soft clay. Int. J. Phys. Model. Geotech. 20 (1), 38–54.
Chen, H.J., Li, X.J., Yan, W.M., Chen, S.C., Zhang, X.M., 2017. Shaking table test of immersed tunnel considering the geological condition. Eng. Geol. 227, 93–107.
Chen, Z.Y., Liu, Z.Q., 2019. Effects of pulse-like earthquake motions on a typical subway station structure obtained in shaking-table tests. Eng. Struct. 198, 109557.
Chen, P.L., Geng, P., Chen, J.B., Gu, W.Q., 2023. The seismic damage mechanism of Daliang tunnel by fault dislocation during the 2022 Menyuan Ms6.9 earthquake based on unidirectional velocity pulse input. Eng. Fail. Anal. 145, 107047.
Chung, Y.T., Sernaker, M.L., 1994. Assessment of target mode selection criteria for payload modal survey. Proceedings of the 12th International Modal Analysis 2251, 272.
Cui, P., Ge, Y.G., Li, S.J., Li, Z.H., Xu, X.W., G, D., Zhou, G., Chen, H.Y., Wang, H., Lei, Y., Zhou, L.B., Yi, S.J., Wu, C.H., Guo, J., Wang, Qi, Lan, H.X., Ding, M.T., Ren, J.J., Zeng, L., Jiang, Y.J., Wang, Y., 2022a. Scientific challenges in disaster risk reduction for the Sichuan–Tibet Railway. Eng. Geol. 309, 106837.
Cui, Z., Li, J.H., Fu, X.W., Sheng, Q., Zhou, G.X., Ma, Y.L.N., Wang, T.Q., 2022b. Evaluating the response of a tunnel subjected to strike-slip fault rupture in conjunction with model test and hybrid discrete–continuous numerical modeling. Rock Mech. Rock Eng. 55 (8), 4743–4764.
Fei, J.B., Wei, J.Y., Khalid, M.I., Zhou, X.S., Li, G.L., Chen, X.S., 2024. Failure of Daliang tunnel induced by active stick–slip fault. J. Rock Mech. Geotech. Eng. https://doi.org/10.1016/j.jrmge.2024.07.007.
Feng, D., 2013. Decomposition based fast least squares algorithm for output error systems. Signal Process. 93 (5), 1235–1242.
Fishman, K.L., Mander, J.B., Richards, R., 1995. Laboratory study of seismic free-field response of sand. Soil Dynam. Earthq. Eng. 14 (1), 33–43.
Gou, Y.X., Huang, Q.B., Liu, N.N., Chen, D.P., Peng, J.B., 2024. Influence of ground fissures on metro shield tunnels: large-scale experiment and numerical analysis. J. Rock Mech. Geotech. Eng. https://doi.org/10.1016/j.jrmge.2024.05.022.
Han, J.Y., Hesham El Naggar, M., Li, L.Y., Hou, B.W., Xu, J.S., Du, X.L., 2020. Design and commissioning of continuous soil box supported on shake tables array for testing long geostructures. Soil Dynam. Earthq. Eng. 132, 106107.
Hu, W., Xin, C.L., Li, Y., Zheng, Y.S., van Asch, T.W.J., McSaveney, M., 2021. Instrumented flume tests on the failure and fluidization of tailings dams induced by rainfall infiltration. Eng. Geol. 294, 106401.
Hu, H.Q., Bao, Y.J., Guo, X.P., Han, X., Gan, G., 2023. Verification of a stochastic dynamic analysis method by shaking table tests of a slope retaining system. Structures 55, 531–544.
Lei, H.Y., Hu, Y., Han, Q.H., Zheng, G., Zhao, B., Du, Y.M., 2020. Design and test verification of a cylindrical 3D laminar shear soil container for use on shaking tables. Soil Dynam. Earthq. Eng. 139, 106384.
Li, Y.D., Zheng, S., Luo, W.L., Cui, J., Chen, Q.R., 2020. Design and performance of a laminar shear container for shaking table tests. Soil Dynam. Earthq. Eng. 135, 106157.
Li, R.H., Zhao, X., Bilotta, E., Zhang, J.H., Zhao, M., Huang, J.Q., Yuan, Y., 2024. Shaking table tests on deformation pattern and failure mechanism of fault-crossing tunnels in non-rupture scenario. Soil Dynam. Earthq. Eng. 180, 108621.
Lombardi, D., Bhattacharya, S., Scarpa, F., Bianchi, M., 2015. Dynamic response of a geotechnical rigid model container with absorbing boundaries. Soil Dynam. Earthq. Eng. 69, 46–56.
Meng, S.B., Li, W.X., Liu, Z.X., Liu, J.Q., He, W.G., Yang, C.W., Zhao, J.W., Wei, S.T., 2024. Rapid resilience assessment framework for mountain tunnels subjected to near-fault seismic ground motions. Soil Dynam. Earthq. Eng. 182, 108746.
Shen, Y.S., Gao, B., Yang, X.M., Tao, S.J., 2014. Seismic damage mechanism and dynamic deformation characteristic analysis of mountain tunnel after Wenchuan earthquake. Eng. Geol. 85–98.
Toda, S., Hataya, R., Abe, S., Miyakoshi, K., 1996. The 1995 Kobe earthquake and problems of evaluation of active faults in Japan. Eng. Geol. 43 (2–3), 151–167.
Vivek, B., Raychowdhury, P., 2019. Design and calibration of a laminar soil box suitable for a low-capacity shake table using free-field tests on Ganga sand. Soils Found. 59 (5), 1602–1612.
Wang, G.B., Ba, F., Miao, Y., Zhao, J.L., 2022. Design of multi-array shaking table tests under uniform and non-uniform earthquake excitations. Soil Dynam. Earthq. Eng. 153, 107114.
Wang, Q., Geng, P., Chen, C.J., Chen, J.B., He, C., 2023a. Determination of seismic response of reinforced tunnel portal slope using shaking table tests. Tunn. Undergr. Space Technol. 136, 105072.
Wang, Q., Geng, P., Li, P.S., Chen, J.B., He, C., 2023b. Dynamic damage identification of tunnel portal and verification via shaking table test. Tunn. Undergr. Space Technol. 132, 104923.
Wen, Y.M., Xin, C.L., Shen, Y.S., Huang, Z.M., Gao, B., 2021. The seismic response mechanisms of segmental lining structures applied in fault-crossing mountain tunnel: the numerical investigation and experimental validation. Soil Dynam. Earthq. Eng. 151, 107001.
Wu, D.H., Liu, Y.Q., Li, H.B., Xia, X., Peng, B., Shen, H., 2020. Shaking table tests on dynamic amplification and failure mechanism of layered rock slopes under seismic actions. Chin. J. Rock Mech. Eng. 39 (10), 1945–1956.
Xin, C.L., Wang, Z.Z., Gao, B., 2018. Shaking table tests on seismic response and

damage mode of tunnel linings in diverse tunnel-void interaction states. Tunn. Undergr. Space Technol. 77, 295–304.
Xin, C.L., Wang, Z.Z., Zhou, J.M., Gao, B., 2019. Shaking table tests on seismic behavior of polypropylene fiber reinforced concrete tunnel lining. Tunn. Undergr. Space Technol. 88, 1–15.
Xin, C.L., Wang, Z.Z., Yu, J., 2020. The evaluation on shock absorption performance of buffer layer around the cross section of tunnel lining. Soil Dynam. Earthq. Eng. 131, 106032.
Xin, C.L., Wang, Z., Hajirasouliha, I., Yang, F., Li, W.H., Gao, B., 2022. Seismic response mechanisms of casing-shape composite tunnel lining: theoretical analysis and shaking table test verification. Tunn. Undergr. Space Technol. 162, 107440.
Xin, C.L., Shuai, Y.X., Song, D.Q., Liu, X.L., 2024a. Dynamic interaction and failure mechanism in tunnel-slope systems: mitigation insights from shaking table tests and numerical analysis. Tunn. Undergr. Space Technol. Tunn. Undergr. Space Technol. 152, 105940.
Xin, C.L., Yang, F., Feng, W.K., Wang, Z., Li, W.H., 2024b. Seismic responses and shattering cumulative effects of bedding parallel stepped rock slope: model test and numerical simulation. J. Rock Mech. Geotech. Eng. https://doi.org/10.1016/j.jrmge.2024.03.031.
Yan, G.M., Shen, Y.S., Gao, B., Zheng, Q., Fan, K.X., Huang, H.F., 2020. Damage evolution of tunnel lining with steel reinforced rubber joints under normal faulting: an experimental and numerical investigation. Tunn. Undergr. Space Technol. 97, 103223.
Yang, C.H., Cheng, P.H., You, J.I., Louis, L.T., 2002. Significant resistivity changes in the fault zone associated with the 1999 Chi-Chi earthquake, west-central Taiwan. Tectonophysics 350 (4), 299–313.
Yang, Y.S., Yu, H.T., Yuan, Y., Sun, J., 2021. 1 g Shaking table test of segmental tunnel in sand under near-fault motions. Tunn. Undergr. Space Technol. 115, 104080.
Yu, H.T., Chen, J.T., Antonio, B., Yong, Y., 2016. Damage observation and assessment of the Longxi tunnel during the Wenchuan earthquake. Tunn. Undergr. Space Technol. 54, 102–116.
Zhang, J.H., Yuan, Y., Yu, H.T., 2019. Shaking table tests on discrepant responses of shaft-tunnel junction in soft soil under transverse excitations. Soil Dynam. Earthq. Eng. 120, 345–359.
Zhang, C.Y., Xu, J.G., Qian, Y.L., Zhang, J.P., Wang, R., Wang, B., 2022. Seismic reliability analysis of random parameter aqueduct structure under random earthquake. Soil Dynam. Earthq. Eng. 153, 107083.
Zhang, Y., Zhang, Z.Q., Yin, C., Wei, R.H., Zhang, H., 2023. Experimental study on forced response characteristics and anti-dislocation performance of articulated tunnel structure under dislocation action of normal fault. Structures 48, 867–881.
Zhang, X., Shen, Y.S., Qiu, J.T., Chang, M.Y., Zhou, P.F., Huang, H.F., Zhu, P.L., 2024. Failure and deformation mode for soil and tunnel structure crossing multiple slip surfaces of strike-slip fault in model test. Soil Dynam. Earthq. Eng. 179, 108541.
Zhao, J.J., Chen, Q., Yang, Y.H., Xu, Q., 2023. Coseismic faulting model and post-seismic surface motion of the 2023 Turkey–Syria earthquake doublet revealed by InSAR and GPS measurements. Remote Sens. 15, 3327.
Zhong, Z.L., Wang, Z., Zhao, M., Du, X.L., 2020. Structural damage assessment of mountain tunnels in fault fracture zone subjected to multiple strike-slip fault movement. Tunn. Undergr. Space Technol. 104, 103527.

Chunlei Xin has been engaged in teaching and research in the field of seismic interaction in geotechnical engineering and underground structural engineering. He obtained his Master degree and PhD in Bridge and Tunnel Engineering from Southwest Jiaotong University in 2011 and 2016, respectively. He pursued joint PhD studies at Rensselaer Polytechnic Institute from 2013 to 2014. Since 2022, he has been working as a researcher at the State Key Laboratory of Geological Hazard Prevention and Geological Environment Protection. He was recognized as a high-level talent in overseas studies from Sichuan Province and the transportation industry. He was also regarded as a key teacher at Chengdu University of Technology. Throughout his career, he has successfully led and participated in over ten research projects funded by the National Natural Science Foundation of China and provincial-level research programs. He has published more than 20 SCI-indexed papers as the first author or corresponding author. His contributions have been acknowledged with a second-class prize for scientific and technological progress at the provincial and ministerial levels.